Doctoral Dissertation

Functional Cellulose Monoliths for Flow-Based Applications

機能性セルロースモノリスのフロー系への応用

Zhaohang Yang

December 2019

Graduate School of Engineering

Osaka University

Contents

General Introduction

Chapter 1.

Cationic functionalization of cellulose monoliths using a urea-choline based deep eutectic solvent and their applications

Chapter 2.

Removal of Cationic or Anionic Dyes from Water Using Ion Exchange Cellulose Monoliths as Adsorbents

Chapter 3.

Cellulose Monoliths Supported Metal/Organic Framework as Hierarchical Porous Materials for Flow Reaction

General Introduction

1. Overview

Biomass is regarded as a carbon-neutral renewable resource that can help reduce greenhouse gas (GHG) emissions. Studies conducted in recent decades on different types of biomass materials have revealed that cellulose, a bio-based polymer, is a feasible substitute for fossil fuels and materials that do not compete with food or feed, considering that its production in the biosphere is thought to be over 7.5×10^{10} tons per year.[1-6] Since its discovery in 1838 by French chemist Anselme Payen,[7] there has been increasing focus on the cross-disciplinary research and use of this copious natural polymer.

Cellulose can be extracted from plant sources, such as cotton, wood and algae, using different physical, chemical, and enzymatic processes. Apart from plants, certain bacteria, algae, and fungi produce cellulose as well. Cellulose is a linear homopolymer that is comprised of β-1,4 linked glucopyranose units containing many hydroxyl groups.[8] These groups form numerous strong inter- and intra-molecular hydrogen bonds (Figure 1) that give cellulose outstanding chemical and physical properties, which permit its use in various forms for a vast range of materials and products.

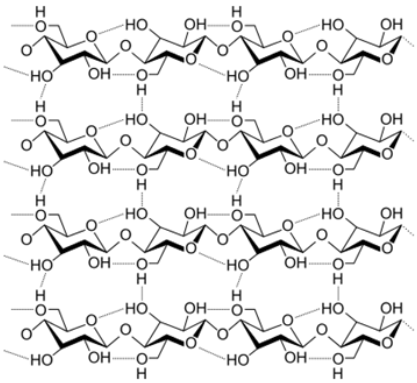

Figure 1. The molecular structure of cellulose with intra- and inter-chain hydrogen bonds.

Looking closely at its molecular structure, cellulose is an active chemical owing to the existence of three hydroxyl groups in each one of the glucose residues. Most reactions of cellulose are associated with these particular hydroxyl groups. The reactivity of the three hydroxyl groups under diverse conditions depends on their intrinsic chemical reactivity and the steric effects of both the reacting agent and the supramolecular structure of cellulose.[9,10]

For many years, cellulose has acted as a raw chemical material for the manufacture of many different products, such as paper, petrochemical, pharmaceutical drugs, cosmetics, textiles, among others. Its widespread use is pegged on the hydrophilicity, biodegradability, biocompatibility, high strength and durability, high thermal stability, low density and low cost of cellulose-based products. Nonetheless, the use of unprocessed cellulose is limited by the strong hydrogen bonds between the inter- or intra-macromolecules, and its lack of particular functions and properties. As a consequence, the modification of cellulose is a vital process, and involves the use on natural renewable cellulose materials to synthesize unique chemicals and products. The modification of the constitution and chemical composition of natural cellulose differs with that of synthetic polymer since the structure and properties of cellulose are ascertained by biosynthesis. One of the modification strategies is chemical modification, which involves the introduction of functional groups into cellulose molecules, giving it new properties without damaging its remarkable intrinsic properties. Chemical modification allows a huge reduction of the high energy consumption linked to cellulose production, as well as the manufacture of end products with desired properties.[11-13] Despite the fact that cellulose is endowed with different intrinsic properties, including high hydrophilicity, high crystallinity, and mechanical strength, chemical modification

can considerably increase its viability in scientific and industrial applications, especially in respect to surface activity and solubility.[14,15]

2. Chemical modification of cellulose

The use of chemical modification of cellulose to give it new properties was first reported in 1870 with the manufacture of the first thermoplastic polymeric material "celluloid" (cellulose nitrate plasticized with camphor) by Hyatt Manufacturing Company.[16] One derivative of cellulose discovered in the 19th century is cellulose nitrate, and it is formed by the esterification of cellulose with nitric acid in the presence of sulfuric acid, phosphoric acid or acetic acid. Today, there are many commercially viable cellulose esters, such as cellulose acetate, cellulose acetate propionate and cellulose acetate butyrate.

Etherification is yet another strategy for chemically modifying the structure of cellulose. Examples of commercially viable cellulose ethers include cellulose acetate, methyl cellulose, carboxymethyl cellulose and the hydroxyalkyl celluloses. A popular etherification strategy is the cationization of the surface of cellulose by applying glycidyltrimethylammonium chloride (GTMAC) or other derivatives. These cellulose esters and ethers have wide application in the manufacture of different products, such as coatings, laminates, optical films, sorption media, pharmaceuticals, foodstuffs and cosmetics. [16]

Another strategy for modifying the structure of cellulose is reacting cellulose with bi- or poly-functional compounds to form cross-linked or resinification products in the cellulose matrix.[17] Cellulose modification was revolutionized by the synthesis of cellulose graft copolymers. Actually, it is possible to obtain polymeric materials with

outstanding properties through graft copolymerization by altering various parameters, such as the polymer type, degree of polymerization and polydispersities of the main chain and the side chains, graft density (average spacing in between the side chains), and the distribution of grafts (graft uniformity). Through graft copolymerization, the preeminent properties of two or more polymers can be integrated in one physical unit.[18-20] This means it is possible to synthesize a graft polymer with properties such as temperature responsiveness,[21] hydrophobicity and oleophobicity,[22] flexibility, sorbancy,[23] ion exchange capability [24] and polarization. [25] Thus, tailor-made graft copolymers can be formed through explicit polymerization methods depending on the target use or specific needs.

The chemical modification of cellulose, for example, by cationic/anionic functionalization, is of particular importance to allow the synthesis of versatile cellulosic materials, such as nitrocellulose, cellulose acetate, and cellulose nanofibrils (CNFs). Such materials are widely used in papermaking, coatings, mineral flotation, composites, biomedicine, cosmetics, and textiles. Recently, deep eutectic solvents (DESs) have been utilized as green media for the pretreatment/modification of cellulose since the majority of them are made up of renewable, biodegradable, and less costly components. However, cellulose was observed to have poor solubility in DESs.

Abbott et al. (2005) first reported the efficient acetylation of monosaccharides and cellulose with acetic anhydride at 90 °C for 3 h in ChCl–ZnCl DES, which acted as both a reaction medium and a catalyst.[26]. Actually, this strategy offers a pretty clean and flexible route to synthesizing cellulose acetate in comparison with the traditional acetylation process that utilizes sulfuric acid as a catalyst, producing cellulose acetate with comparatively poor mechanical properties. It is also worth noting that available

hydroxyl groups in cellulose could also be reacted with the DES component to synthesize cationic-functionalized cellulose with improved hydrophilicity (Scheme 1). [27]

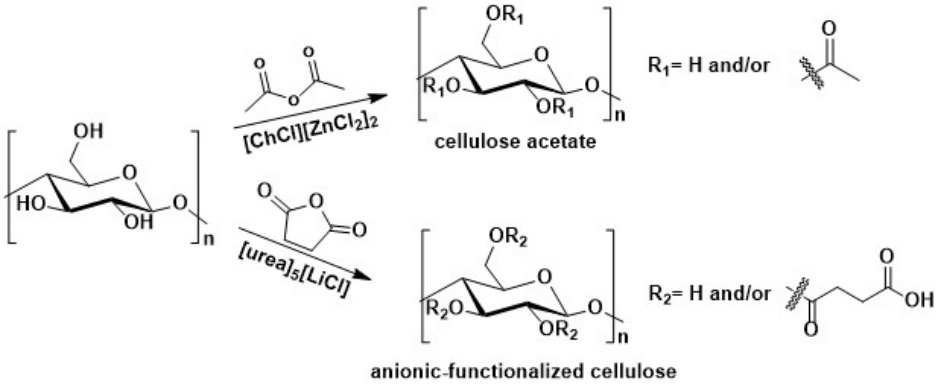

Scheme 1. Acetylation and anionic functionalization of cellulose in DESs. [26,28]

The chemical modification of cellulose through anionic functionalization could also be performed by catalyst-free succinylation with succinic anhydride in urea–LiCl DES at 70–80 ℃ for 2 h. Negatively charged groups (carboxyl groups) in the modified cellulose significantly enhanced electrostatic repulsion and structural swelling between cellulose fibers, which fostered the nanofibrillation of cellulose to obtain CNFs with diameters ranging from 2–7 nm. After the anionic functionalization of cellulose, just a small decrease in the degree of polymerization (DP) and crystallinity index (CrI) was noted.[28]

3. Polymer monolith

Over the last decade, numerous chemical materials have been developed, and one such material is porous polymer monoliths (PMs). PMs are synthesized via a simple molding process conducted inside a closed mold. It is easy to mold PMs into different shapes and sizes, including thin layers, columns and microfluidic channels.

Polymerization of a mixture that is comprised of monomers, free-radical initiators, and a porogenic solvent results in macroporous materials with big through-pores that are highly valuable in flow-through applications.[29-32] This preparation technique is quite versatile especially when used with hydrophobic, hydrophilic, ionizable, and zwitterionic monomers. It is also possible to regulate the porous properties of the monolith over a broad range. This also makes it possible to ascertain the hydrodynamic properties of devices made with molded media. Considering that the entire mobile phase will obviously flow through the monolith, mass transport inside the molded material is mainly influenced by convection. Monolithic devices have been noted to produce good performance even at extremely high flow rates. An example of the application of such materials is in the chromatographic separation of biological compounds and synthetic polymers, as well as electrochromatography, gas chromatography, enzyme immobilization, molecular recognition, and advanced detection systems. Using certain polymers to graft pore walls realizes materials with fully modified surface chemistries.[33-39]

Monolithic porous cellulose has often served as a separation media in column chromatography, ion-exchange chromatography, and affinity chromatography, among others. Mostly, cellulose monoliths are practical materials that have a continuous 3D framework within a single unit. Owing to their 3D structure, cellulose monoliths usually have a large surface area, which provides for quick mass transfer of reagent solution, justifying their application as a feasible medium in a number of fields. Research on the preparation of cellulose monolith is limited, particularly in regard to its preparation process, mechanical properties, and structural property. It is vital for monoliths to be synthesized via a method with clear-cut controllability in morphology and reproducibility since monolith properties, including the biodegradation rate, hydrophilicity and

adhesiveness, are largely dependent on its pore and skeletal size. Hence, a method with process flexibility is required so as to obtain formation that is desirable and suitable for each usage.

Lately, the outstanding versatility, simplicity, and pore size controllability of the phase separation technique has made it popular than other methods. Additionally, the remarkable processability of this method makes it feasible considering that the shape of monoliths is determined by the shape of molds in areas where phase separation and gelation takes place. The preparation method for cellulose monoliths can be divided into two based on the type technique used to trigger phase separation: non-solvent induced phase separation (NIPS) and thermally induced phase separation (TIPS).

Lloyd et al. has provided details about these techniques based on the Flory-Huggins theory.[40,41] In sum, changes in the polymer fraction in a ternary system of polymers, good solvents, and non-solvents leads to an increment of Gibbs free energy, thereby triggering phase separation. Phase separation continues till the lowest Gibbs free energy up to the moment the mixing of polymer-lean and polymer-rich phases stabilizes. Depending on the composition and temperature of the mixture, the system may undergo liquid-liquid and/or solid-liquid phase separation, which influences the final morphology of monoliths. It has been established that liquid-liquid phase separation results in an interpenetrating 3-D network caused by spinodal decomposition, while solid-liquid phase separation results in sea-island morphology, including polymer precipitation resulting from nucleation and growth mechanism.

Thermally induced phase separation has been applied in the preparation of cellulose monoliths. In this method, the reduction in polymer solubility caused by the solution temperature normally triggers phase separation. Different from the NIPS process,

TIPS has good reproducibility and flexibility properties considering that phase separation is influenced by simple temperature reduction instead of non-solvent exchange including variables, which require to be controlled. Furthermore, the morphology can be controlled by altering a variety of factors, including the particular solvent, solvent ratios, polymer concentration, molecular weight, and quench temperature. Further, the TIPS process can be applied to a broad range of materials, including semi-crystalline polymers with no soluble solvent at room temperature. Normally, a good/poor binary solvent helps induce phase separation and gelation through the solubility gap during quenching. In Uyama's group, cellulose monoliths with high porosity have been fabricated based on the template-free TIPS method (Figure 2). It is possible to adjust the pore size of cellulose monoliths by altering solvent ratios, polymer concentration, and quenching temperature.

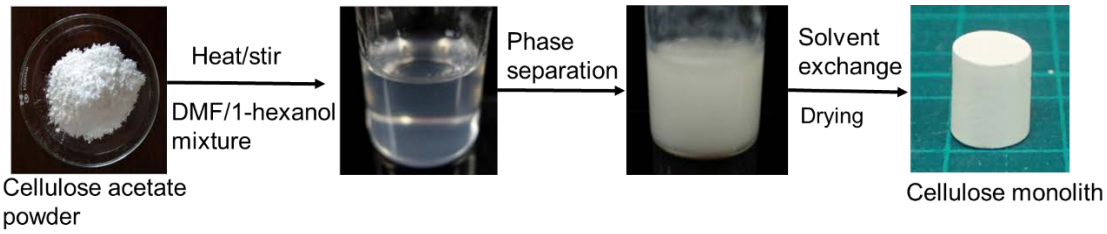

Figure 2. A general protocol for preparation of cellulose monolith by TIPS method.

4. Functional composite monolith

Metal−organic frameworks (MOFs), also referred to as porous coordination polymers, represent a new range of highly ordered porous crystalline materials made up of infinite ordered arrays of metal-ion-based nodes (or clusters containing metals), which have been linked by polydentate organic linkers to form extended networks. Due to the nature of their interactions, rational and versatile assemblies between metal centers and organic ligands allow the tuned MOF to have structural and chemical flexibility. This

gives them a number of remarkable properties, like ultrahigh large surface areas, crystalline nature, tunable pore sizes and shapes, high porosity, and specific adsorption affinities. Nowadays, more attention is being given to MOFs because of their capacity for application in such areas as separation, catalysis, sensors, energy conversion/storage, electrochemistry and biomedicine. [42-44]

In-depth research has been conducted to investigate ways of integrating MOF on solids (e.g., polymer materials, metal or metal oxide particles, plastic, silica etc.).[45-47] Notably, the coated MOF layers allow the manufacture of "smart" surfaces, which can be modified based on the desired functionality. In particular, the structure of micro- or nanocrystalline MOF layers over proper porous polymer supports provides for the formation of a large variety of new composite materials with a wide range of properties.[48,49] When the MOF layers are assembled on a substrate, they demonstrate to have both intrinsic microporosity and mesoporosity, which can be respectively attributed to the internal crystalline structure and the spatial arrangement of individual building units.[50] MOF engineering for specific applications has attracted a lot of research attention in recent times. However, there is little research on flow-based applications that utilize porous polymer materials coated with MOFs. This is possibly because of the inappropriate morphology and small particle size of MOFs, which can make them inappropriate for packing in flow-through supports. Combined with the advantages of PMs mentioned above, they are considered as outstanding supports for conjugation of MOFs.

In conclusion, it is clear that the cellulose monolith has many advantages, but its use is still limited mainly because of its lack of functional groups. Furthermore, pristine cellulose monoliths have physical properties that are meant for specific applications,

especially in flow-through technology. Therefore, it is quite necessary to create cellulose-based functional monoliths, which can be utilized to open the cellulose monoliths toward flow-based techniques and contribute to the sustainable society.

5. Contents of this thesis

This doctoral thesis is related to the development of functional cellulose monoliths and study of their applications in flow-based mode. It consists of 3 chapters and the core contents are summarized as follows.

Chapter 1

An alternative green strategy based on non-toxic and readily biodegradable chlorocholine chloride/urea deep eutectic solvents, which act both as functionalization agents and solvents that allow for the cationization of cellulose monoliths was investigated. The influence of deep eutectic solvent modification on the properties of the resulting monoliths was demonstrated by SEM, FTIR, elemental analysis, TGA and BET surface area analysis. The prepared cationized cellulose monoliths performed as novel adsorbents were explored for the adsorption of acid red 70 anionic dye, and their adsorption ability and recyclability were also studied. The present cationized cellulose monolith has potential in the adsorption of anionic dyes due to the charge- induced adsorption aided by quaternary ammonium groups.

Chapter 2

Poly(sodium *p*-styrenesulfonate) (PSS) and poly[(3-acryloylaminopropyl)-trimethylammonium chloride] (APTAC) modified ion exchange cellulose monoliths (C-*g*-PSS and C-*g*-APTAC, respectively) were fabricated and employed for the removal

of cationic or anionic dyes from aqueous solutions with particular reference to the effects of initial dye concentration, flow rate and ionic strength on adsorption. Dynamic adsorption performance and recyclability were carefully discussed. Furthermore, the permeability and back pressure of the prepared ion exchange cellulose monoliths was also observed comparing with pristine cellulose monolith at different flow rates.

Chapter 3

This chapter demonstrates a quick and highly effective pump injection strategy for preparing macro-porous chemically modified cellulose monoliths for which the pore surface is coated with ZIF-8 metal organic framework (MOF). Pore surface coverage with the microporous ZIF-8 resulted in an obvious increase in surface area from 19 to 262 $m^2 g^{-1}$. Monolithic polymer coating with ZIF-8 was implemented as catalysis microreactor for the Knoevenagel condensation reaction, the catalytic activity and reusability were discussed. Moreover, the application in fast and efficient preconcentration of trace levels of toxic chlorophenols in waters was also demonstrated. The obtained nanoparticle/polymer monoliths have the desirable hierarchical porous structure and functional properties, which can significantly extend the use of composite cellulose monoliths, especially in flow-based mode.

Cellulose-based functional or composite monoliths are expected to maintain the superior chemical and physical properties of cellulose monolith and meanwhile exerting the functional properties of modification moieties. Author hopes these functional cellulose monoliths with desired properties will find promising applications in various fields of flow-based mode.

6. References

1. Gatenholm P, Klemm D, *MRS Bull*, 2010, **35**, 208–213.
2. Habibi Y, Lucia L A, and Rojas O J, *Chem Rev*, 2010, **110**, 3479–3500.
3. Siro´ I, Plackett D, *Cellulose*, 2010, **17**, 459–494.
4. Eichhorn S J, *Soft Matter*, 2011, **7**, 303–315.
5. Eichhorn S, Dufresne A, Aranguren M, *Mater Sci*, 2010, **45**, 1–33.
6. Klemm D, Kramer F, Moritz S, *Angew Chem Int Ed*, 2011, **50**, 5438–5466.
7. Payen A, Hebd C R, *Seances Acad Sci*, 1838, **7**, 1052–1056.
8. Wakelyn P J, Bertoniere N R, French A D, *Handbook of Fiber Chemistry*, 1998, 577-721.
9. Tegge G, Hebeish A, *Starch-Stärke*, 1981, **33**, 432-432.
10. Faruk O, Bledzki A K, Fink H P, *Progress in polymer science*, 2012, **37**, 1552-1596.
11. John M J, Anandjiwala R D, *Polym Compos*, 2010, **29**,187-207.
12. Klemm D, Kramer F, Moritz S, et al. *Angew Chem Int Ed*, 2011, **50**, 5438-5466.
13. Fang L, Zhang X, Ma J, *RSC Adv*, 2015, **5**, 45654-45661
14. Habibi Y, *Chem Inform*, 2014, **45**(20),1519-1542.
15. Eichhorn S J, Dufresne A, Aranguren M, *J Mater Sci*, 2010, **45**, 1-33.
16. Klemm D, Heublein B, Fink HP, *Angew Chem Int Ed*, 2005, **44**, 3358-3393.
17. Nevell T P, Zeronian S H, *Cellulose chemistry and its applications*, 1985, 384-422.
18. Stevens M P, *Polymer Chemistry*, New York: Oxford univ. 1999.
19. Odian G, *Principles of Polymerization*, John Wiley & Sons, 2004.
20. Bhattacharya A, Misra B N, *Prog Polym Sci*, 2004, **29**, 767-814.
21. Chausan G S, Mahajan S, Guleria L K, *Desalination*, 2000, **130**, 85-88.
22. Wang Z, Zhang Y, Jiang F, *Polym Chem*, 2014, **5**, 3379-3388

23. Gupta K C, Khandeka K, *Biomacromolecules*, 2003, **4**, 758-765.

24. Hebeish A, EI-Hilw Z H, *J. Appl. Polym Sci*, 1998, **67**, 739-745.

25. O-Rak K, Ummartyotin S, Sain M, Manuspiya H, *Mater Lett*, 2013, **107**, 247-250.

26. Abbott A P, Bell T J, Handa S, *Green Chem*, 2005, **7**, 705-707.

27. Abbott A P, Bell T J, Handa S, *Green Chem*, 2006, **8**, 784.

28. Selkala T, Sirviç J A, Lorite G S, *ChemSusChem*, 2016, **9**, 30743083.

29. Huang N, Drake H, Li J, *Angew Chem Int Ed Engl*, 2018, **57**, 8916-8920.

30. Shih Y, Wang K, Singco B, *Langmuir*, 2016, **32** , 11465-11473.

31. Svec F, Lv Y, *Anal Chem*, 2014, **87**, 250-273.

32. Nischang I, Causon T *J, Trends Analyt Chem*, 2016, **75**, 108-117.

33. Nischang I J, *Chromatogr A*, 2012, **1236**, 152-163.

34. Pang J, Liao Y, Huang X, *Talanta*, 2019, **199**, 499–506.

35. Darder M, Salehinia S, Parra J B, *ACS Appl Mater Interfaces*, 2017, **9**, 1728-1736.

36. Lawson S, Hajari A, Rownaghi A A, *Sep Purif Technol*, 2017, **183**, 173-180.

37. Jacobson G B, Shinde R, Contag C H, *Angew Chem Int Ed*, 2008, **47**, 7880-7882.

38. Liu C, Wong G M, Yeung K W K, *Polymers*, 2016, **8**, 287-306.

39. Mikos A G, Thorsen A J, Czerwonka L A, *Polymer*, 1994, **35**, 1068-1077.

40. Lloyd D R, Kinzer K E, Tsng H S J, *Membr Sci*, 1990, **52**, 239-261.

41. Lloyd D R, Kim S S, Kinzer K E J, *Membr Sci*, 1991, **64**, 1-11.

42. Liu J, Wöll C, *Chem Soc Rev*, 2017, **46**, 5730-5770.

43. Yuan S, Feng L, Wang K, *Adv Mater*, 2018, **30**,1704303.

44. Li B Y, Bux H, Feldhoff A, *Adv Mater*, 2010, **22**, 3322–3326.

45. Lv Y, Tan X, Svec F J, *Sep Sci*, 2017, **40**, 272-287.

46. Fu Q, Wen L, Zhang L, *ACS. Appl Mater Interfaces*, 2017, **9**, 33979-33988.

47. Lirio S, Liu W, Lin C, *J Chromatogr A*, 2016, **1428**, 236-245.

48. Wen L, Gao A, Cao Y, *Macromol Rapid Commun*, 2016, **37**, 551-557.

49. Ghani M, Masoum S, Ghoreishi S M, *J Chromatogr A*, 2018, **1567**, 55-63.

50. Iacono M, Connolly D, Heise A, *RSC Adv*, 2017, **7**, 19976-19981.

Chapter 1.

Cationic functionalization of cellulose monoliths using a urea-choline based deep eutectic solvent and their applications

1.1 Introduction

As described in general introduction, chemical modification can significantly decrease the high energy consumption associated with cellulose production and it also allows the production of end products with desired functionalities. Cationic surface functionalization of cellulose with ammonium or amino functional groups has proven to have immense value for a wide range of applications, such as efficient adsorption, separation and analysis of macromolecules. The most common cationization methods involve the introduction of an ammonium group by reacting the hydroxyl group of polysaccharide with 2,3-epoxypropyltrimethylammonium chloride in an alkaline solution.[1,2] An alternative method involves the generation of the reagent in situ from (3-chloro-2-hydroxypropyl)trimethylammonium chloride and sequential periodate oxidation.[3,4] However, these methods usually have several ineluctable drawbacks, such as consuming large amounts of organic solvents, resulting in low yields and loss of products in the reaction process. Besides the well-grounded environmental and health concerns, consumed organic compounds generally lead to the hard challenge of costly separation and impose negative effects to the environment.

In accordance with the currently prevailing green chemistry, researchers in the area of chemistry and chemical engineering are being encouraged to adopt greener

methodologies in chemical synthesis.[5,6] Deep eutectic solvents have been heralded as the most promising environmentally benign replacement solvents and reagents for some more volatile organic compounds in chemical and industrial processes. They can be obtained by simply mixing two or more chemical elements together to realize a solution with a lower melting point than any of the original elements.[7-11] Nonetheless, the possibility of utilizing DESs as alternative solvents for modification and functionalization applications in cellulose has not received the desired attention in the literature. In order to make headway in this area of research, a novel method aiming to functionalize cellulose is proposed in this study.

In this chapter, cationized cellulose monoliths (CMs) were prepared for separating anionic molecules by utilizing deep eutectic solvent based on chlorocholine chloride and urea as the reaction media for a cost-effective, efficient and eco-friendly cellulose monolith cationization. Chlorocholine chloride was used in the reaction as a cationization reagent. The adsorption technique of anionic dyes was used to investigate the anion exchange properties. On the other hand, kinetics and isotherm modeling of adsorption experimental data as a function of time, flow rate and initial concentration was performed to predict the adsorption mechanism and capacity.

1.2 Experimental

Chemicals and materials

Commercially available cellulose acetate (CA) with molecular weights (M_n=5.0×10^4; 39.7 wt.% acetyl content), 1-hexanol, urea and chlorocholine chloride (CCC) were obtained from Sigma-Aldrich Co.Y. Sodium hydroxide was purchased from Wako Chemicals (Osaka, Japan). *N*, *N*-dimethyl formamide (DMF) was supplied by

Nacalai Tesque, Inc. (Kyoto, Japan). Acid red 70 was purchased from TCI, Ltd. (Tokyo, Japan). Deionized (DI) water was used when water is involved. All chemicals and reagents were of analytical grade and used without further purification.

Preparation of CM

CM was prepared by deacetylation of cellulose acetate (CA) monolith which was fabricated via thermally induced phase separation (TIPS) method. Firstly, CA monolith was produced by completely dissolving 2 g of CA powder into 10 mL of a good solvent DMF followed by adding 15 mL of poor solvent 1-hexanol dropwise until the mixtures becoming transparent, the whole process was operated at 85 ^{o}C with continuous and gentle stirring for 3 h. Then the mixture was transferred into a desired mold and maintained at 20 ^{o}C for 12 h to complete phase separation. After the formation of the monolith prototype, solvent exchange was thoroughly completed using methanol. The cellulose monolith was then obtained by hydrolyzing the CA monolith with 0.5 mol L^{-1} sodium hydroxide methanol solution at room temperature for 3 h. Finally, the monolith was successively washed with DI water and methanol, and then vacuum dried at room temperature.

Surface quaternization of DES treated cellulose monolith

Chlorocholine chloride/urea deep eutectic solvent (CCC/urea DES) was prepared using previously reported method by heating the mixtures of chlorocholine chloride and urea powders at mole ratio of 1:2 with constant stirring at 80 °C until a homogeneous clear viscous liquid had formed.[12,13] Subsequently, cationization reaction was carried out by treating cellulose monolith in this medium with 6wt.% of NaOH which is acting both as solvent and reactant. The optimized conditions involved reaction of

cellulose monolith for 8 h at 95 °C. The DES-modified cellulose (CCC/urea-c) monolith was then washed copiously with DI water and dried in vacuum at room temperature. During the cationization reaction, the trimethylammonium groups were incorporated onto cellulose through nucleophilic addition of the alkali-activated hydroxyl groups of cellulose to the chloride moiety of chlorocholine chloride, as shown in Scheme 1-1.

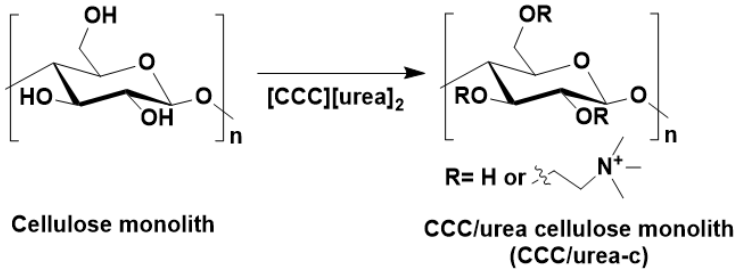

Scheme 1-1. Schematic diagram of CCC/urea-c monolith.

Characterization

The morphologies of all samples were investigated by scanning electron microscopy (SEM) (Hitachi SU3500, Japan) with an accelerating voltage of 10kV. Fourier transform infrared spectrophotometry (FT-IR) (Thermo Scientific Nicolet iS 5, USA) and CHN corder elemental analyzer (YANACO MT-5) were used to confirm the successful cationization of CM. Thermal stability was assessed by thermogravimetric analysis performed with STA 7000 Thermogravimetric Analyzer (Hitachi, Japan) by applying the heating rate of 10 ^{o}C in an inert nitrogen atmosphere. Nitrogen adsorption/desorption isotherms were measured with a NOVA 4200e surface area & pore size analyzer (Quantachrome Instruments) at 77 K. The specific surface area was calculated based on the method of Brunauer-Emmett-Teller (BET) equation. The monoliths' mechanical response towards compressive stress were recorded on a table-top material tester (Shimadzu EZ Graph, Japan) at room temperature using a 500 N load cell

at 5 mm min^{-1} compression rate.

Permeability

Considered in many experimental studies, permeability is an intensive property of a porous medium and it is a measure of the capacity of the medium to transmit fluids.[14] The concept of permeability is of paramount importance in the petrochemical industry in that it can be used to measure the resistance of a fluid.[15] The apparatus schematic diagram used for permeability is shown in Scheme 1-2.

As a permeable material, the monolith was tightly fitted with a heat shrink tubing before heating. The shrunken diameter was smaller than the monolith's diameter, and the loaded monolith was connected to a digital quantitative tubing pump (DSP-100SA, As One, Japan) and a digital pressure gauge (KDM30) by polypropylene tubing. This was done to ensure a constant flow rate. Next, the monolith was rinsed with water before each measurement to ensure stability at a constant flow rate. Normally, permeability is considered absolute because regardless of the working fluid, the permeability coefficient K depends on only the structure of the porous medium. Darcy's law defines the equation of permeability in terms of measurable quantities,[16]

$$B_0 = \frac{L \times v \times \mu}{\Delta P} \qquad (1)$$

$$v = \frac{q}{A} \qquad (2)$$

in which L is the length of monolith (cm), v is the linear velocity of a given fluid in flow system (cm s^{-1}), μ is the viscosity of fluid (Pa·s), q is flow rate (mL s^{-1}), A is cross sectional area to flow (cm^2), B_0 is permeability of porous medium, Darcy (1 Darcy=1×10^{-8} cm^2), ΔP is the pressure drop when influent flowing through the monoliths (Pa).

Dynamic adsorption experiments and recyclability

Two types of adsorption studies on the laboratory scale have been used, namely batch mode[17,18] and continuous flow mode. [19] Batch operation is not a suitable method at the industrial scale to deal with high flow rates for the reason that most of the treatment systems, contact time is not sufficiently long for the attainment of equilibrium and therefore the data obtained are generally not applicable. From an industrial point of view, removal of dyes using continuous flow system is an effective and reliable process for treating large-scale wastewater volumes and cyclic adsorption/desorption.[20-22] In such mode of operations, all the active sites on the adsorbent are occupied, and the adsorbent is used completely. This presents several advantages including operational simplicity, ability to handle large influent flow rates, high yields and scaling up of the processes. Nevertheless, very few studies have been done to validate the removal of dyes in continuous flow mode.

There are single-charged monatomic anions of Cl^- based on the chemical structure of the DES-modified cellulose monolith. As organic base groups, quaternary ammonium cations have a binding preference for anions. Therefore, anionic dyes can be adsorbed on the DES-modified cellulose monolith via an anion-exchange process. The monolith was assembled as mentioned above. The effluents were time-resolved measured with UV/Vis detector (Infinite M200, Tecan, Japan) at 568 nm. Before the experiment, the monolith system was equilibrated with deionized water.

A typical cyclic operation of adsorption and desorption was carried out as follows. In the adsorption stage, a sufficient amount of acid red 70 dye solution (initial concentration = 30 ppm, 50 ppm or 70 ppm) was pumped through the monolith at a constant flow rate (1, 2 or 3 mL min^{-1}). Immediately after the adsorption trials, desorption

experiments were carried out with a mixture of ethanol, sodium chloride and water for 30 min at the flow rate of 3 mL min^{-1}, thereby regenerating the monolith. Each cyclic operation was repeated five times to evaluate the monolith regenerability under flow conditions. All the experiments were conducted at room temperature, and the effects of the initial influent concentration and flow rate on the monolith column performance were analyzed.

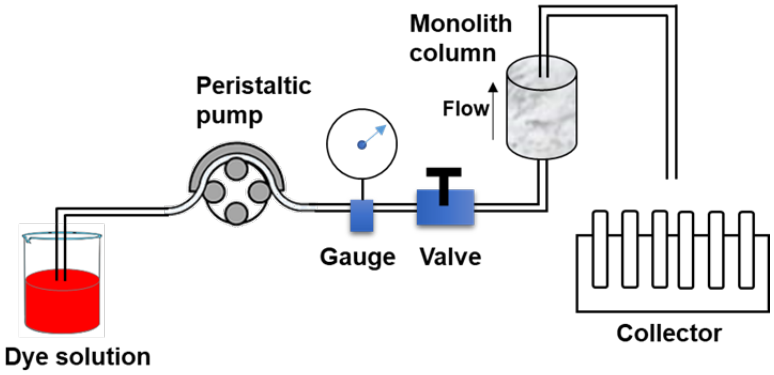

Scheme 1-2. Schematic diagram of operation for dynamic system assays.

Mathematical analysis of dynamic adsorption

The performance of the monolith can be evaluated based on the shape of breakthrough curve obtained by plotting effluent concentration versus time of treatment.[21] In order to evaluate dye removal capacity, it was determined equilibrium capacity (q_e) and useful removal capacity (q_u) by the equation 3 and 4, respectively,

$$q_e = \frac{C_0 Q}{1000m}\int_0^{t_e}\left(1-\frac{C_t}{C_0}\right)dt \qquad (3)$$

$$q_u = \frac{C_0 Q}{1000m}\int_0^{t_b}\left(1-\frac{C_t}{C_0}\right)dt \qquad (4)$$

where, q_e is the equilibrium adsorption amount of dye at saturation point per unit mass

of adsorbent in mg g^{-1}, q_u is the useful removal amount at break point concentration per unit mass of adsorbent in mg g^{-1}, C_0 is the initial concentration of dye (ppm), Q is the flow rate (mL min^{-1}), m is the mass of adsorbent (g), C_t is the collected effluent concentration of dye at time t (ppm), t_e is the exhaustion time , t_b is the time to breakthrough point, t_e and t_b are all experimentally obtained (min). The plot of adsorbed dye concentration (1- C_t / C_0) versus time (t , min) gives area above the breakthrough curve.

Total amount of dye sent to monolith (M_t) during useful removal stage was obtained from equation 5,

$$M_t = \frac{C_0 Q t_e}{1000} \qquad (5)$$

where, M_t is the total amount of dye sent to the monolith in mg.

Another feature of the breakthrough curves is the mass transfer zone (*MTZ*), which is defined as the adsorbent zone where the active adsorption happens. It is the most common and frequently used parameter using the linear driving force approximation for designing adsorption monoliths and the analysis of sorption kinetics from a breakthrough curve. It is far preferable to obtain the length of *MTZ* (*MTZL*) from small-scale laboratory experiments on the adsorbate-adsorbent system under consideration. A convenient equation 6 to calculate the *MTZL* is,

$$MTZL = \left(1 - \frac{t_b}{t_s}\right) \cdot L \qquad (6)$$

where, *L* is the length of the entire monolith (cm).

Finally, for each flow rate, the total dye removal percentages are determined as the ratio between equilibrium capacity (q_e) and the total amount of dye passing through the monolith to saturation as shown in equation 7.

$$Total\ dye\ removal\ (\%) = \frac{q_e \cdot m}{M_t} \times 100 \qquad (7)$$

Modelling of breakthrough curves

It is important for an optimal design in industrial adsorption process by analyzing the experimental data and simulating the dynamic behavior and performance of adsorption system. Predict the breakthrough curve of dynamic adsorption by using mathematical models. The shape of this curve is determined by the shape of the equilibrium isotherm and influenced by the individual transport process in the monolith. In this work, the dynamic behavior of the monolith was predicted and analyzed with two models i.e. (i) Thomas model and (ii) Yoon-Nelson model.

The Thomas model

The Thomas model is one of the most general and widely used model for the description of performance theory in the adsorption processes, which external and internal diffusion constraints are not present. It demonstrates that the flow rate driving force obeys the second order reversible reaction kinetics and the Langmuir isotherm. The expression computes the maximum concentration of solute on the adsorbent and the adsorption rate constant for an adsorption column. The linearized form of the model can be described by the following equation 8,

$$\ln\left[\left(\frac{C_0}{C_t}\right) - 1\right] = \left(\frac{K_{Th} q_e m}{Q} - K_{Th} C_0 t\right) \qquad (8)$$

where, K_{Th} is the Thomas rate constant (mL min^{-1} mg^{-1}), q_e is the theoretical equilibrium dye adsorbed per gram of the adsorbent (mg g^{-1}) and m is the amount of adsorbent in the column (g). Q is the flow rate of the influent solution through the column (mL min^{-1}). The kinetic constants K_{Th} and the q_e can be determined from the linear plot of $\ln((C_0/C_t) - 1)$ versus t at a given flow rate.

The Yoon-Nelson model

Yoon-Nelson model is very simple and straightforward model, which doesn't demand any information related to the property of adsorbate, adsorbent type, and the physical property of the adsorption system. The Yoon-Nelson model is principally based on the belief that the rate of decrease in the probability of adsorption for each adsorbate molecule is proportional to the probability of adsorbate adsorption and the probability of adsorbate breakthrough on the adsorbent. The linearized form of Yoon-Nelson model for a single component system is expressed as:

$$\ln \frac{C_t}{C_0 - C_t} = K_{YN} t - \tau K_{YN} \qquad (9)$$

where, K_{YN} is the rate constant (min^{-1}) and τ is the time required for 50% adsorbate breakthrough (min). The values of parameters K_{YN} and τ for the adsorbate can be calculated from the plot of $\ln(C_t/(C_0 - C_t))$ versus sampling time (t) according to equation 9.

1.3 Results and discussion

Morphology and composition of functionalized CM

Figure 1-1. shows the cross-sectional SEM images of CM with and without deep eutectic solvent modification. The unreacted CM had a continuous three-dimensional (3D) porous network built of highly cross-linked clusters that are aggregated and assembled into an interconnected structure (Figure 1-1 a, b). This skeletal structure is typical of monolith obtained through thermally induced phase separation processes. The effect of DES functionalization is obviously observable (Figure 1-1 c, d). Cationic modification with the aid of DES resulted in the interconnected fibrillar skeleton compared to the virgin CM. Taking this into account, it is reasonable to assume that the vast majority of the

available hydroxyl groups on the cellulose have been functionalized. Although the size of the pore and skeleton slightly decreased, the morphological features of primeval 3D network CM were well-sustained even after modification under strong alkali conditions. Current conditions are preferable for the cationic functionalization in that they will not solubilize the monolith dramatically.

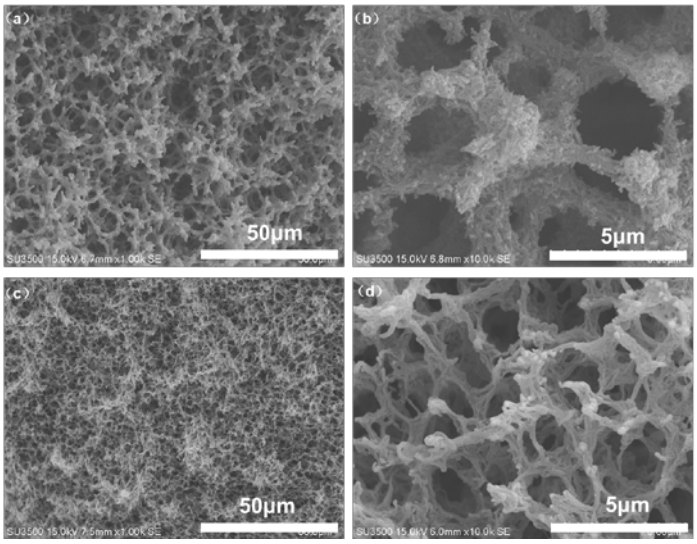

Figure 1-1. SEM images of the cross-section at different scale for **(a, b)** CM; **(c, d)** CCC/urea-c monolith.

For the purpose of further confirming the inner architectures, nitrogen adsorption and desorption measurements of two types of monoliths were carried out, as shown in Figure 1-2. Both of the curves can be classified as type IV isotherm with adsorption hysteresis loops in terms of IUPAC classification, suggesting the characteristic of mesoporous materials (2-50 nm). A pronounced hysteresis loop of type H1 was observed in the P/P_0 ranging from 0.6 to 1 for the CM, while the hysteresis of DES-modified CM starting at $P/P_0 \approx 0.8$ demonstrated sharp capillary condensation, suggested the presence of meso-pores and macro-pores. Pore size distribution curves (inset of Figure 1-2) are important factors for mass transport. The pore size distribution of the monoliths were

calculated by employing a practical method according to Density Functional Theory (DFT) that is based on a molecular model for adsorption of nitrogen in porous solids. A sharp peak around 4.9 nm was observed in both monoliths. This reveals that mesopores which is beneficial for the adsorption of macromolecules are dominant for the monolith.

The specific surface areas, pore volumes and average pore diameters were analyzed based on nitrogen adsorption and desorption measurements (see Table 1-1). There is no remarkable decrease of BET specific surface area which is around 400 $m^2 g^{-1}$, for DES-modified cellulose monolith compared with pristine cellulose monolith. It suggests that some mesopores are closed during the cationization processes. The slightly decreased pore volume and pore size can be explained by the functionalization of DES that some voids of monolith disappeared. These two parameters are also key factors affecting the surface area. Despite this, sufficient surface area, pore volume, and pores of DES-modified cellulose monolith provide abundant binding sites for the anion exchange with target molecules.

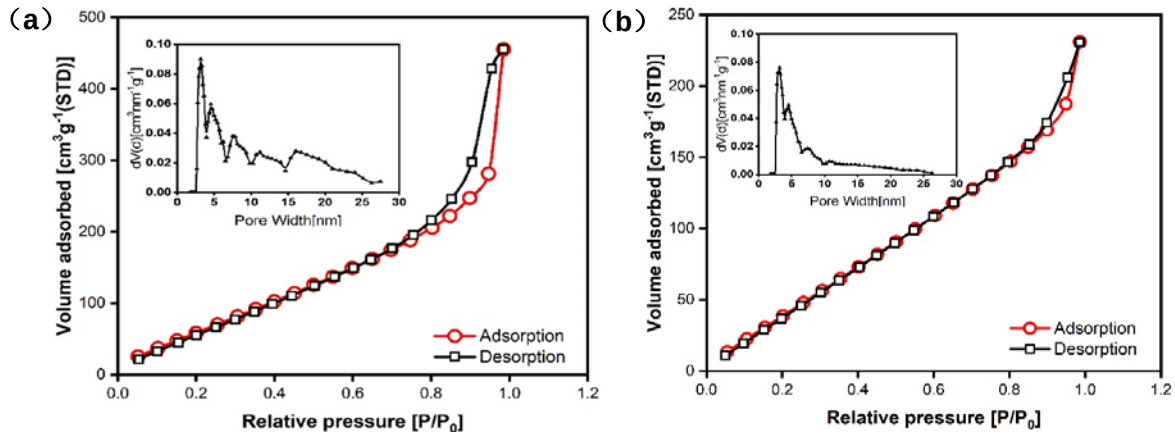

Figure 1-2. Nitrogen adsorption/desorption isotherms of **(a)** CM and **(b)** CCC/urea-c monolith. Inset: pore size distribution plots.

Table 1-1. Porous parameters comparison of CM and CCC/urea-c monolith.

sample	Surface area ($m^2 g^{-1}$)	Total Pore volume ($cm^3 g^{-1}$)	Average pore diameter (nm)
CM	416	0.71	6.86
CCC/urea-c	402	0.48	4.78

To determine if the DES-modified cellulose monolith had been obtained, FTIR spectroscopy procedure was performed to investigate surface chemistry (see Figure 1-3 a). Reference sample at around 3400, 2900, 1430, 1371, and 899 cm^{-1} are the characteristic absorptions of native cellulose. Compared with the reference sample, distinctive absorption bands at around 1660, 1620, 1480 and 770 cm^{-1} appeared in the spectra of DES-modified cellulose monolith, assigned to the characteristic bands, namely amide C–O stretching vibration, amide NH scissoring band, $C–N^+$ symmetric stretching vibration and N–H bond out-of-plane bending band, which confirmed the occurrence of the nucleophilic addition reaction between cellulose hydroxyl groups and DES. In addition, elemental analysis revealed there was 3.01% nitrogen by mass in the DES-modified cellulose monolith (Table 1-2). The presence of nitrogen confirmed that the desired product had been obtained successfully.

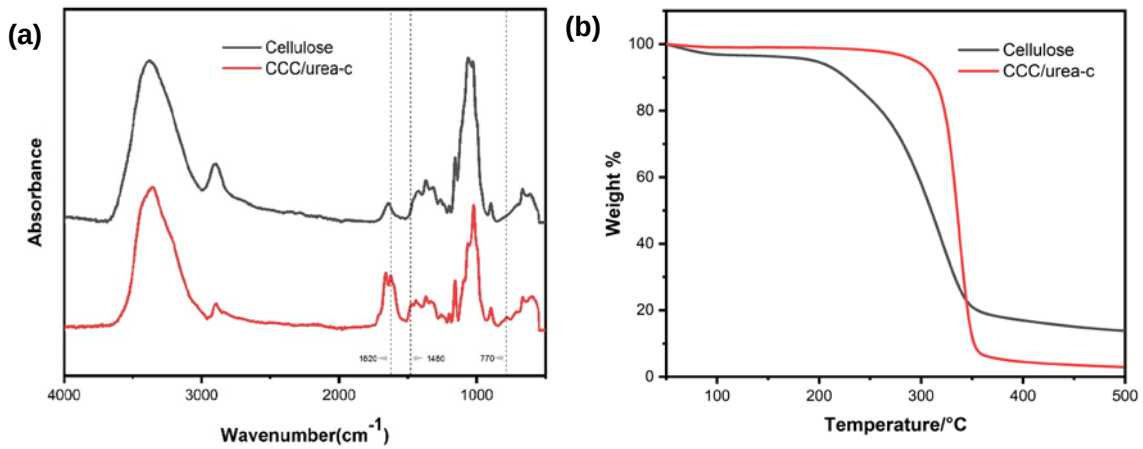

Figure 1-3. (a) FT-IR spectra of cellulose monolith and CCC/urea-c monolith; **(b)** TGA curves of cellulose monolith and CCC/urea-c monolith.

Table 1-2. Elemental composition of monolith samples

Sample	Carbon (%)	Hydrogen (%)	Nitrogen (%)
CM	40.69	6.30	0.00
CCC/urea-c	40.80	6.31	3.01

Thermogravimetric analysis (TGA) curves of cellulose monolith and DES-modified cellulose monolith are shown in Figure 1-3 b. The DES-modified one is more hydrophilic than unmodified one. The initial gradual weight loss of DES-modified cellulose monolith decreased by 5% at approximately 100 ^{o}C indicated the moisture evaporation. After 100 ^{o}C, the weight remained constant until the initial temperature of combustion was reached. The combustion profiles of the samples indicated a higher thermal stability for cellulose monolith than the DES-modified one. The initial temperature of cellulose monolith combustion was 320 ^{o}C. However, the effect of DES functionalization was observable for the cationized cellulose monolith whose initial temperature of combustion was at 265 ^{o}C. During this stage, the cellulose and cationized ones were almost completely burnt out because of the destruction of the crystalline structure and oxidative thermal degradation. The temperature difference (55 ^{o}C) between the cellulose monolith and the DES-modified one indicates the DES functionalization effects on the intermolecular forces and hydrogen bonding. It was also observed that the weight loss stopped after higher limit combustion temperature and some residual materials remained for all samples. These residues indicated the carbon purity of the samples. The higher weight residue of DES-modified cellulose monolith was probably due to the grafted ammonium salt.

Stress-strain behavior

Uniaxial compression deformation tests were performed to evaluate the changes

in the mechanical strength. Figure 1-4 shows the influence of cationization on the compression properties of the monolith under both dry and wet conditions. Under wet condition, both monoliths show a low modulus plateau before a linear elastic deformation. The compression strains corresponding to the indicator of linear elastic deformation starting at 0.01 MPa stress (noted as 0.01) are summarized to compare the compression properties of these monoliths (see Table 1-3). The ε0.01 increased significantly after cationization, indicating that cellulose monolith can sustain larger deformation after DES modification. The maximum strain of DES-modified cellulose monolith can go beyond 80% with a compression modulus of 1.5 kPa. The cellulose monolith exhibits a higher compression modulus of 4.7 kPa but it is fractured at a strain of 68.6% with a fractured stress of 0.3 MPa. The monoliths consist of flexible 3D network of cellulose and demonstrate a ductile behavior throughout the strain function. Also important is that highly flexible DES-modified cellulose monolith can bend into a thin slice without collapsing; therefore, the phenomenon helps in folding and twisting the cationized cellulose monolith. Under dry conditions, the compressive modulus of the cellulose monolith remained at 6.0 kPa after DES modification. At low strains (< 5%), the stress-strain behavior was linearly elastic in nature. Thus the deformation was expected to be primarily due to elastic cell wall bending. In higher strain, the stress–strain behavior showed a horizontal plateau region after reaching a yield stress. After the cationization, the range of the plateau regime decreased under compressive conditions. The plateau regime is associated with the collapse of the skeleton under compressive loading. When the skeleton of the monoliths has almost collapsed, the opposing skeleton is connected, and further strain compresses the solid itself. This process produced the final region of rapidly increasing stress.

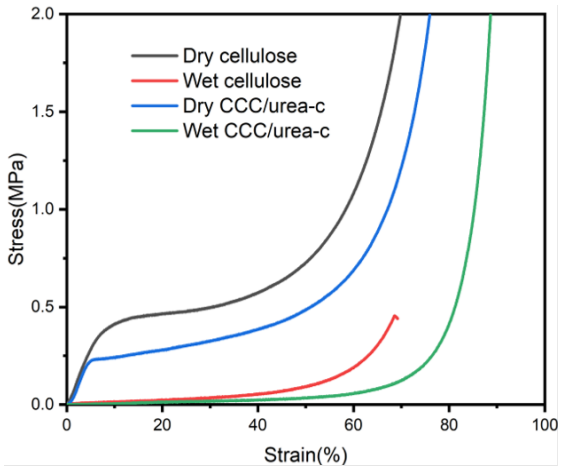

Figure 1-4. Compression stress-strain curves of CM and CCC/urea-c monolith.

Table 1-3. Mechanical properties of monoliths before and after cationic functionalization under wet and dry conditions.

Sample	Compression modulus* (kPa)	Fractured strain (%)	Compression strength (MPa)	Strain at 0.01 MPa stress (%)
Dry cellulose	6.0±0.1	-	-	-
Wet cellulose	4.7±0.2	68.6±3.2	0.5±0.3	16.5±4.2
Dry CCC/urea-c	6.0±0.1	-	-	-
Wet CCC/urea-c	1.5±0.1	-	-	36.5±1.5

Evaluation of Permeability

Furthermore, the absolute permeability was analyzed to evaluate the intensive property of monolith in the flow system. To calculate the monolith permeability coefficient B_0 in the flow system, the average measurements of pressure loss at flow rate of 1, 2 and 3 mL min^{-1} respectively were used. The pressure loss was also analyzed using the average of the three measurements to reduce deviation caused by backpressure fluctuations. Based on the data obtained from Table 1-4, it can be noticed that the pressure drop increases as the flow rate increases across the monolith. After increasing the flow rate from 1 to 3 mL min^{-1}, the pressure drop values were noted as 6.5-19.7 kPa for the

cellulose monolith and 7.3-22.4 kPa for the DES-modified one. Therefore, the pressure drop is proportional to the runoff of the liquid through the monolith. When plotting the pressure drop against flow rate (see Figure 1-5), the straight line shows the relationship between these properties. It was also noticed that the DES-modified cellulose monolith exhibits a little lower permeability compared with unmodified ones. As shown in the SEM images, the pore size decreased after the cationization modification. This is because the changes in the complex pore structure and the pore characteristic (porosity and pore radius) determined the decreased permeability. Despite this, DES-modified cellulose monolith is effective and viable for flow-through applications due to its highly sufficient permeability. For non-compressible fluids, the permeability of the monolith is maintained irrespective of the type of fluid that flows through it. For this reason, author analyzed the effect of length on pressure drop based on the obtained permeability coefficient of the monolith (see Table 1-5). It is clear that there was a linear increase in the pressure drop. Thus, length design is also a vital element in practice as it ensures that the structure of the monolith will not collapse in the event of significant pressure drop.

Table 1-4. Permeability comparison of CM and CCC/urea-c monolith.

	q (mL min^{-1})	v (cm s^{-1})	Pressure drop ΔP (kPa)	Permeability* B_0 (D)
CM				
	1	0.059	6.5	0.81
	2	0.118	13.1	0.80
	3	0.177	19.7	0.80
CCC/urea-c				
	1	0.059	7.3	0.72
	2	0.118	14.8	0.71
	3	0.177	22.4	0.70

*Permeability is calculated at i.d.=6 mm, L=10 mm by pressure drop obtained from average of 3 measurements.

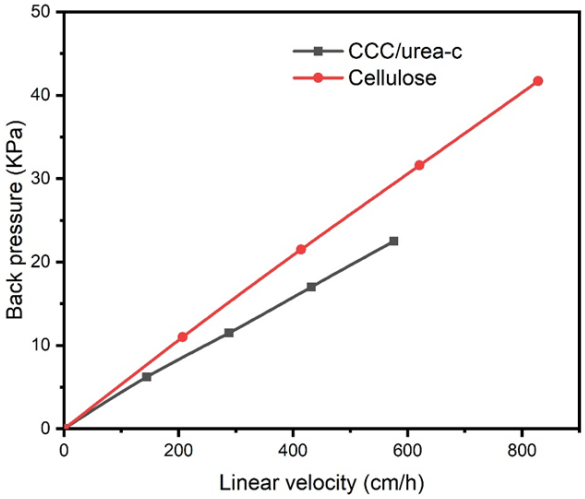

Figure 1-5. Comparison of pressure drop of cellulose monolith and CCC/urea-c monolith at different linear velocity.

Table 1-5. Calculated pressure drops at different length of monoliths.

	L (cm)	*v* (cm s^{-1})	Pressure drop* *ΔP* (kPa)	Permeability B_0 (D
CM				
	2	0.059	13.1	
	3	0.059	19.6	0.80
	5	0.059	32.7	
CCC/urea-c				
	2	0.059	14.8	
	3	0.059	22.2	0.71
	5	0.059	36.9	

* Pressure drop is calculated at i.d.=6 mm, flow rate of 1 mL min^{-1} by average permeability coefficient obtained from flow rates of 1, 2 and 3mL min^{-1}

Dynamic adsorption by continuous flow system and monolith regeneration studies

Effect of flow rate

Dynamic assays were performed to investigate the effect of various flow rates (of 1.0 to 3.0 mL min^{-1}) on breakthrough curves through a monolith of 1 cm in length and

an influent dye concentration of 30 ppm at ambient temperature, as shown in Figure 1-6 a and all parameters are summarized in Table 1-6. The breakthrough curve shows a reduction in breakthrough and saturation times with increasing the flow rate from 1.0 to 3.0 mL min^{-1}. At low flow rate, the dye has more time to contact with adsorbent resulting in a better adsorption capacity and higher removal efficiency from solution. The highest total dye removal (82.4%) and experimental adsorption capacity (23.1 mg g^{-1}) were obtained at the lowest flow rate of 1mL min^{-1}. At higher flow rate, conversely, the curve is close to breakthrough time at 3 mL min^{-1} from the very beginning of the assay. That may have occurred due to dye solution residence time in the monolith was not enough to reach the adsorption equilibrium. The highest *MTZL* value and the lowest removal amount and removal percentages were obtained at 3 mL min^{-1} flow rate assay. The variation in the slope of the breakthrough curve and adsorption capacity may be explained on the basis of mass transfer fundamentals. The reason is that at higher flow rate, the mass transfer rate gets increased, namely the amount of dye adsorbed onto unit monolith length

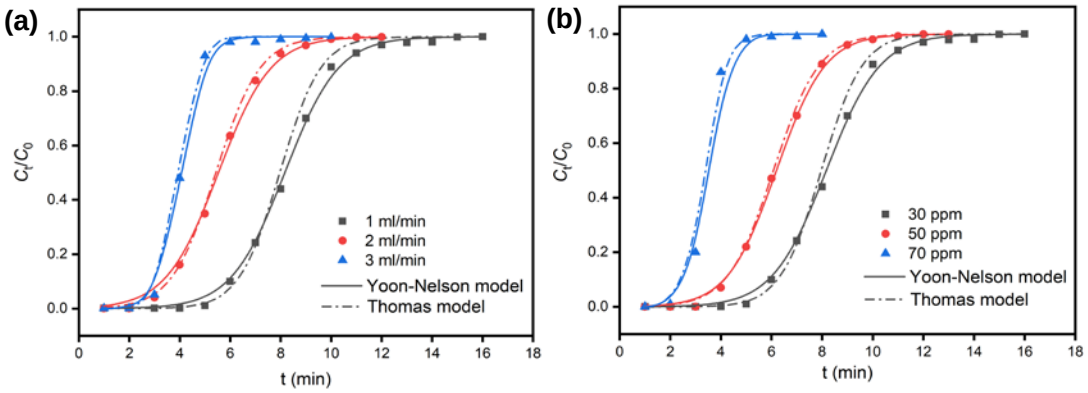

Figure 1-6. Experimental and predicted breakthrough curves of acid red 70 adsorption by CCC/urea-c monolith predicted by the Thomas and Yoon-Nelson model **(a)** at different flow rates (C_0=30 ppm, L=1cm); **(b)** at different initial concentration (flow rate=1 mL min^{-1}, L=1 cm).

Table 1-6 Experimental data and parameters obtained at different operating conditions

C_0 (mg L^{-1})	Q (mL min^{-1})	t_b (min)	t_s (min)	q_e (mg g^{-1})	q_u (mg g^{-1})	M_t (mg)	*MTZL* (cm)	*Removal* (%)
30	1	6.0	15.0	23.1	14.8	0.18	0.60	82.4
30	2	3.6	10.4	22.7	12.0	0.22	0.65	77.8
30	3	2.8	8.2	22.2	12.6	0.25	0.66	75.0
50	1	4.1	11.4	28.0	17.0	0.21	0.64	82.9
70	1	1.8	6.2	29.2	17.5	0.13	0.71	83.3

gets increased with increasing flow rate leading to faster saturation, and thus the monolith active life is significantly reduced. It is worthy to be considered that a lower value is chose as the influent flow rate for removal of the dyes in the practical application.

Effect of initial concentration

To evaluate the effect of initial inlet concentration on breakthrough curves, three initial feed solutions (30, 50, and 70 ppm) of acid red were used, with the monolith length of 1 cm and an optimum flow rate of 1 mL min^{-1} at ambient temperature. The results are shown in Figure 1-6 b and the breakthrough analysis was summarized in Table 1-6. As shown from the plots and the table, the equilibrium time and the breakthrough time all decreased with the initial dye concentration increasing, respectively. It is easy to find that the breakthrough time became earlier at high concentration, which was explained by the fact that more adsorption sites were available and occupied at higher concentration. It also can be explained by the theories that lower concentration gradient caused slow transport of the acid red dye to the surface of the adsorbent due to decreased diffusion coefficient and a decreased mass transfer driving force. The steepness of curves determines the monolith efficiency to reach saturation. The steeper curves have shorter mass transfer zone which is necessary for

the better monolith performance. The results demonstrate that solutions with the greatest initial concentration (70 ppm) give the highest *MTZL* values and removal percentages (close to 83%). The adsorption capacity and percent removal signify the extent to which active sites are occupied during the adsorption. Moreover, a higher adsorption capacity is obtained with the concentration of 70 ppm, which may be attributed to higher influent concentration providing higher driving force for the transfer process to overcome the mass transfer resistance. This trend is due to the decrease in the total of dye solution passed through the monolith with the increase of the influent dye concentration, until the column reaches to equilibrium time. Therefore, the diffusion process is concentration dependent.

Modelling of the Breakthrough Curves

The Thomas Model

As can be seen in Table 1-7, the value of q_e increased and the value of K_{Th} decreased with an increase in the initial dye concentration. The maximum adsorption capacity q_e decreased and K_{Th} increased with an increase in the flow rate. Based on these, it can be concluded that a lower flow rate, and a higher initial concentration results in better adsorption performance. From Figure 1-6, it can be seen that the experiment values and the predicted values derived from the Thomas model remarkably close to all the experimental conditions. The regression coefficient is higher than 0.9996, a value that attests to the validity of the model for all conditions. This shows that the model predicts the adsorption process well. The model is generally suitable for describing the processes in which internal diffusion has no influence in determining the rate.

Yoon-Nelson Model

The values of K_{YN} and τ obtained from the Yoon-Nelson model are presented in

Table 1-7. It was found that with the flow rate and influent dye concentration increasing, the values of K_{YN} increased and the 50% adsorbate breakthrough time τ decreased. The increase in K_{YN} with flow rate shows a decrease in the mass transfer resistance, and thus, an increase in the driving force required for the mass transfer in the monolith. It can also be observed that the calculated values are close to the experimental values (*t*, exp).

By comparing the R_2 of the two models, it is confirmed that Thomas model provides a better fit to the experimental data.

Table 1-7. The Thomas model and Yoon-Nelson model parameters obtained at different experimental conditions

Parameter	Thomas model			Yoon-Nelson model		
	K_T (mL min^{-1} mg^{-1})	q_e (mg g)	R^2	K_{YN} (min^{-1})	τ (min)	R^2
Flow rate (mL min^{-1}) C_0=30ppm						
1	0.047	28.9	0.9961	1.016	8.16	0.9716
2	0.049	23.8	0.9952	1.042	5.53	0.9879
3	0.119	22.7	0.9996	2.766	4.05	0.9808
Initial concentration (mg L^{-1}) flow rate=1 mL min^{-1}						
30	0.047	28.9	0.9961	1.016	8.16	0.9716
50	0.025	27.1	0.9986	1.139	6.19	0.9983
70	0.021	29.5	0.9908	2.866	3.52	0.9967

Desorption and recyclability

The effective stability and regeneration ability of the adsorbent are essential standards for practical applications. Therefore, research on the reusability of the adsorbent is strongly required. Fast and efficient desorption experiments were carried out using the mixtures of ethanol, sodium chloride and water desorption agent for regenerating the DES-

modified cellulose monolith.[22] An adsorption experiment at a flow rate of 1mL min^{-1} and initial concentration of 70 ppm was used for the recyclability analysis. In the elution process, almost all the adsorbed dyes could be desorbed at flow rate of 3 mL min^{-1} within 30 min. Moreover, the mass transfer effect may have accelerated the desorption efficiency. The recyclability of the CCC/urea-c monolith was investigated by repeating the adsorption-desorption process for five times. The adsorption capacity hardly changed for the first three times. The adsorption ratio was still high. After five successive cycles, the dye removal dropped from 83% to 72% (see Figure 1-7). These data clearly demonstrate that the CCC/urea-c monolith has a remarkably efficient regeneration capability even after multiple reuses.

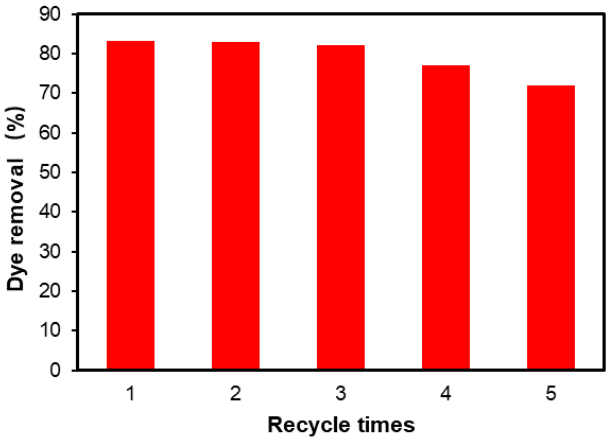

Figure 1-7. Regeneration test of CCC/urea-c monolith using the mixtures of ethanol, sodium chloride and water for 5 cycles. (C_0:70 ppm, 25 °C, desorption time:30 min).

1.4 Conclusion

The cationized cellulose monolith was prepared by the cationization of cellulose with a simple synthesis using a chlorocholine chloride/urea DES as a reaction medium. By producing cellulose monolith, the feasibility of the current cellulose cationization

method in the material application was demonstrated. Because of the quaternary ammonium salts that were modified on the surface of the newly synthesized cellulose monolith have many benefits in anionic reactive dye removal, such as saving time and energy. Moreover, high dye recoveries were achieved using appropriate desorption conditions (mixtures of ethanol, sodium chloride and water). It was also found that this monolith exhibited great adsorption capacity and that it could bind with the anionic dyes quickly and strongly. Moreover, the dye removal process only consumed no more than 1 hour to complete the adsorption and desorption cycle under a negligible pressure drop. Other advantages include the low cost, efficient monolith reusability. The simpler large-scale design for ion exchange monolith-scale-up can be easily achieved by enlarging the monolith while the applied pressure is still low.

1.5 References

1. Aihua P, Nuria B, Lars A, *Soft Matter*, 2013, **9**, 2047-2055.
2. Sehaqui H, Perezd L U, Tingaut P, *Soft Matter*, 2015, **11**, 5294-5300.
3. Prado H J, Matulewicz M C, *Eur Polym J*, 2014, **52**, 53-75.
4. Liimatainen H, Suopajärvi T, Sirviö J, *Carbohydrate Polymers*, 2014, **103**,187-192.
5. Qi H, Chang C, Zhang L, *Green Chem*, 2009, **11**, 177-184.
6. Ma W, Yan S, Meng M, *J Appl Polym Sci*, 2014, **131**, 131.
7. Smith E L, Abbott A P, Ryder K S, *Chem Rev*, 2014, **114**,11060-11082.
8. Del Monte F, Carriazo D, Serrano M C, *ChemSusChem*, 2014, **7**, 999-1009.
9. Wagle D V, Zhao H, Baker G A, *Acc Chem Res*, 2015, **45**, 2299-2308.
10. Wang J, Han J, Khan M Y, *Polym Chem* 2017, **8**, 1599-1738.
11. Zhang Q, Vigier K D O, Royer S, *Chem Soc Rev*, 2012, **41**, 7108-7146.

12. Andrew P A, Thomas J B, *Green Chem*, 2006,**8**, 784-786.

13. Wibowo D, Lee C K, *Biochem Eng J*, 2010, **53**, 44-51.

14. Sharma S, Siginer D A, *Appl Mech Rev*, 2010, **63**, 020802-1- 020802-19.

15. Millington R J, Quirk J P, *Trans Faraday Soc*, 1961, **5**, 1200-1207.

16. Aminu M D, Ardo B U, *J Pet Environ Biotechnol*, 2015,**6**, 2157-7463

17. Zambare R S, Song X, Sowrirajalu B N, *ACS Sustain Chem Eng*, 2017, **5**, 6026-6035.

18. Liu C H, Wu J S, Chiu H C, *Water Res*, 2007, **41**, 1491-1500.

19. Freitas E D D, Almeida H J D, Vieira M G A, *J Clean Prod*, 2017, **171**, 613-621.

20. Akar S T, Uysal R, *Chem. Eng. J*, 2010, **162**, 591-598.

21. Mohammed N, Grishkewich N, Waeijen H A, *Carbohydr Polym*, 2016, **136**, 1194-1202.

22. Xing T, Kai H, Chen G, *Color Technol*, 2012, **128**, 295-299.

Chapter 2.

Removal of Cationic or Anionic Dyes from Water Using Ion Exchange Cellulose Monoliths as Adsorbents

2.1 Introduction

Industrial effluents which are mostly in the form of waste water contaminated with dyes pose unprecedented environmental threat especially when they are discharged into the hydrosphere. Chemically, these dyes can be classified as either anionic or cationic based on their chemical structure.[1] Many of dyes are toxic and potentially carcinogenic.[2] Therefore, it is a health priority to decolorize and eliminate dyes from raw industrial wastewater. Adsorption/ion exchange to dye contaminants has been explored with a broad range of reactive dyes.

Most commercial ion exchangers are in the form of porous particles in packed-bed operation for flow process.[3-7] This type of column has limitations such as low accessible flow rate, and high pressure drop. A promising alternative for eliminating the above problems is macroporous ion exchange monolith. The flow-through porous monolith are beneficial due to the hydrodynamic advantage over conventional columns such as lower pressure drop and enhanced mass transfer. All these play a critical role in speed and scale-up of flow-through applications. Besides, the ion exchange monolith formed by natural organic polymer cellulose also exhibits the advantages of superior chemical stability, facile chemical modification and free modeling.

In this work, natural renewable cellulose are utilized in the manufacture of the

cost-effective, efficient and eco-friendly ionization cellulose monolith adsorbents. These adsorbents have desired functionalities and immense value for removing both anionic and cationic dyes. Methylene blue was used as a model cationic dye which employed by industries such as textile, leather and biomedicine for a variety of purposes.[8] Acid red 70 as a model anionic dye is problematic due to its bright color, acidity and water-soluble reactive characteristic. Sodium p-styrenesulfonate and (3-acryloylaminopropyl)trimethy-llammonium chloride were used as anionization and cationization reagents in the simple radical polymerization, respectively. The dynamic adsorption technique of dyes was used to investigate the ion exchange properties. The kinetics and isotherm modeling of adsorption experimental data as a function of time, flow rate and initial concentration was performed to study the adsorption mechanism and capacity. Furthermore, the influence of ionic strength of the dye solution on the adsorption was also investigated in dynamic method.

2.2 Experimental

Chemicals and materials

Ammonium persulfate were obtained from Sigma-Aldrich Co.Y. Triethylamine were supplied by Nacalai Tesque, Inc. (Kyoto, Japan). Acryloyl chloride (AC), sodium *p*-styrenesulfonate, (3-acryloylaminopropyl)trimethy- lammonium chloride (APTAC), sodium hydroxide, hydroquinone, sodium chloride and calcium chloride were all purchased from Wako Chemicals (Osaka, Japan). Acid red 70 and methyl blue, from TCI, Ltd. (Tokyo, Japan), were used in the dye adsorption studies.

Preparation of ion exchange monoliths

Modification of CM with AC

Acryloyl group-introduced cellulose monolith (ACCM) was synthesized by condensation reaction of hydroxyl group of CMs and acryloyl chloride. Appropriate amount of dried CMs (anhydrate glucose unit around 0.012 mol) were added into a 100 mL eggplant flask containing sufficient DMF which immersed all the samples. Then, distilled triethylamine (0.18 mol) was added into the mixture of CMs and DMF. After stirring for 3 h, excess AC (10:1 molar ratio to the hydroxy groups in cellulose) was added dropwise to the mixture while stirring in an ice bath. The reaction was conducted at room temperature for 24 h. After that, the resultant products were thoroughly washed with DI water.

Grafting of PSS from ACCM

The PSS was grafted from ACCM via free-radical polymerization by using ammonium persulfate as initiator. In this study, 1mol L^{-1} of sodium *p*-styrenesulfonate and 1.0 mol% of ammonium persulfate (corresponding to sodium *p*-styrenesulfonate) were added in the mixture of ACCMs and DI water. The mixture was well homogenized by stirring for 5 h at room temperature to infiltrate PSS into ACCMs and sufficiently deaerated by using a vacuum pump. Then the free-radical polymerization was initiated by transferring the mixture into a 70 °C oil bath. The polymerization was continued for 24 h. After the reaction, the obtained cellulose composite monoliths (C-*g*-PSS) were completely washed with DI water before characterizations.

Grafting of APTAC from ACCM

Cationic CM was synthesized by free-radical polymerization, based on ACCM, 1mol L^{-1} of APTAC with 1.0 mol% VA-044 (corresponding to APTAC) as an initiator. The polymerization reaction was carried out in a 50 °C constant temperature bath

equipped with a mechanical stirrer within an inert (N_2) atmosphere for 6 h and terminated by adding 2 mL saturated hydroquinone solution. After the reaction, the monolith was thoroughly washed with DI water to obtain APTAC grafted cellulose monolith (C-*g*-APTAC), which was then vacuum dried. The details of the synthesis of C-*g*-PSS and C-*g*-APTAC monoliths are summarized in Scheme 2-1.

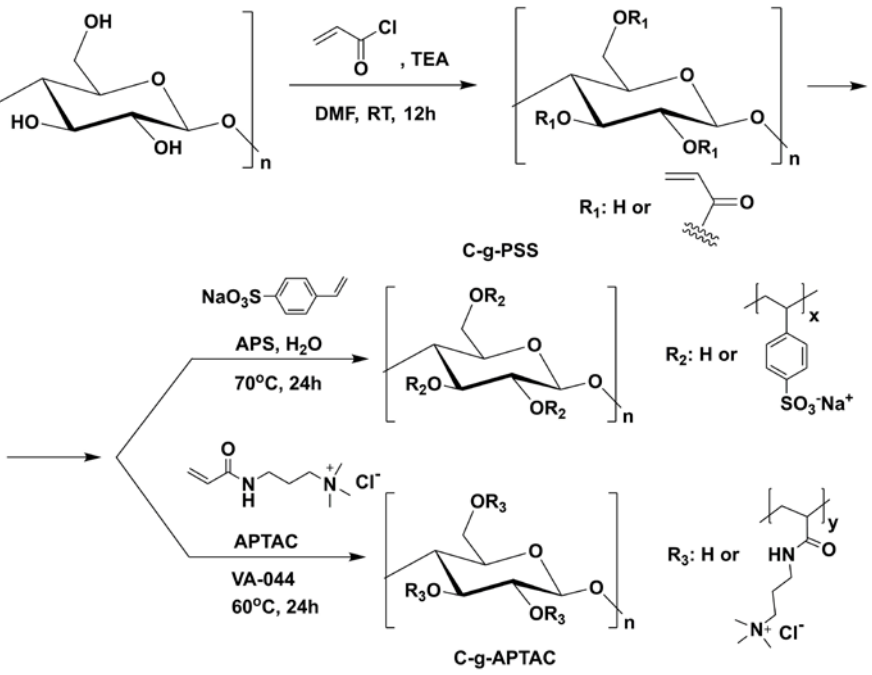

Scheme 2-1. Preparation of C-*g*-PSS and C-*g*-APTAC monoliths.

Determination of the percentage of grafting (PG%)

The composition of C-*g*-PSS and C-*g*-APTAC monoliths were determined as following. The initial weight of the used pristine CM was first recorded before modification. In order to calculate the *PG%* of C-*g*-PSS or C-*g*-APTAC, the wet weight and dried weight of corresponding composite monoliths were measured. The ratio of water (R_w), cellulose (R_c), grafting percentage of PSS or APTAC in monoliths were determined according to equations (1), (2) and (3), respectively,

$$R_w\% = \frac{w_0 - w_d}{w_0} \times 100\% \qquad (1)$$

$$R_c\% = \frac{w_c}{w_0} \times 100\% \qquad (2)$$

$$PG\% = \frac{w_d - w_c}{w_0} \times 100\% \qquad (3)$$

where, w_0 and w_d are the wet weight and dried weight of the monoliths, respectively. w_c is the weight of cellulose in monoliths. With regard to the pristine CM, w_c is exactly the w_d. The w_c in C-*g*-PSS and C-*g*-APTAC monoliths was estimated on the basis of initial CM weight.

Characterization

The morphologies of all samples were assessed by scanning electron microscopy (SEM) (Hitachi SU3500, Japan) with an accelerating voltage of 10 kV. Fourier transform infrared spectrophotometry (FT-IR) (Thermo Scientific Nicolet iS 5, USA), CHNS elemental analyzer (2400II, PerkinElmer, Walth-am, MA, USA) were used to confirm the successful modification of cellulose monolith and obtain the amount of polymer on the monolith surface. Nitrogen adsorption/desorption isotherms were measured with a NOVA 4200e surface area & pore size analyzer (Quantachrome Instruments) at 77 K. The specific surface area was calculated based on the method of Brunauer-Emmett-Teller (BET) equation.

Permeability

Details have been described in Chapter 1.

Dynamic adsorption experiments and recyclability

As organic base groups, quaternary ammonium cations of C-*g*-APTAC monolith have a binding preference for anions, while sulfonate anions of C-*g*-PSS have a binding

preference for cations. This means that anionic dyes can be adsorbed on the C-*g*-APTAC monolith via an anion-exchange process and that cationic dyes can be adsorbed on the C-*g*-PSS monolith via a cation-exchange process. Time-resolved measurements of the effluents were taken using an UV/Vis detector (Infinite M200, Tecan, Japan) at 568 nm for acid red 70 and 668 nm for methylene blue.[9] The monolith system was equilibrated with deionized water prior to the start of the experiment.

The process of adsorption and desorption entailed the following. In the adsorption stage, an adequate amount of acid red 70 dye solution (initial concentration = 75 ppm, 100 ppm or 200 ppm) or methylene blue dye solution (initial concentration = 300 ppm, 500 ppm or 700 ppm) was pumped through the monolith at a constant flow rate (1, 2 or 3 mL min^{-1} for acid red 70 adsorption and 1, 2 or 4 mL min^{-1} for methylene blue adsorption). To regenerate the monolith, desorption experiments were carried out right after the completion of the adsorption trials using appropriate desorption agents for a period of 10 min at a flow rate of 3 mL min^{-1}. This cyclic operation was repeated seven times to examine the regenerability of the monolith under different flow conditions. All the experiments were carried out at room temperature, and the effects of the initial influent concentration, flow rate and ionic strength of dye solutions on monolith performance were analyzed.

Mathematical analysis of dynamic adsorption

The dynamic response of the monolith was appraised based on the breakthrough curve generated by plotting effluent concentration versus time of treatment. Dye removal capacity, exhaustion capacity (q_e), useful removal capacity (q_u), and total dye removal were mathematically analyzed in this chapter. Details have been described in chapter 1.

2.3 Results and Discussion

Morphology and composition of functionalized cellulose monolith

The cross-sectional micrographs of CM and modified CM are shown in Figure 2-1. It can be seen that the pristine CM has a continuous three-dimensional porous network built of highly cross-linked clusters that are aggregated and assembled into an interconnected structure (Figure 2-1 a). For the ACCM (Figure 2-1 b), C-*g*-PSS (Figure 2-1 c) and C-*g*-APTAC (Figure 2-1 d) monoliths, the skeletal structures are well-maintained; however, the pore size of the modified CM as well as the average diameter of the monolith skeleton increased, which results in an increase in the volume of the monoliths as shown in Figure 2-2.

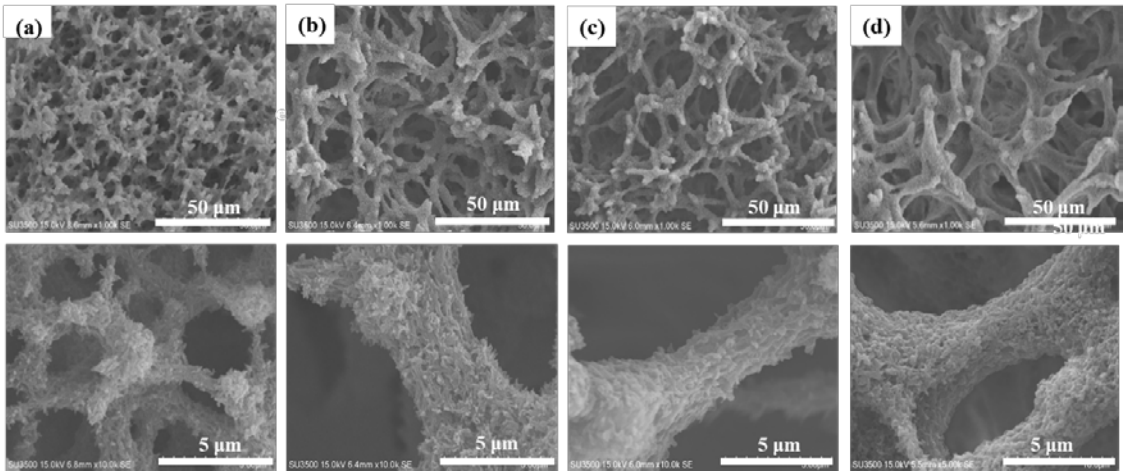

Figure 2-1. SEM images of the cross-section at different scale for **(a)** CM; **(b)** ACCM; **(c)** C-*g*-PSS and **(d)** C-*g*-APTAC monolith.

After modification with AC, the diameter of pristine CM was changed from 5.1 mm to 6.3 mm, and further increased to 7.3 mm and 7.1 mm after grafting with PSS and APTAC, respectively. And the length of ACCM, C-*g*-PSS and C-*g*-APTAC were increased to 6 mm, 7.0 mm and 6.9 mm, respectively, compared to CM with a length of 5 mm. The increase of volume and the reduction of roughness of the skeleton may be

attributed to the acryloyl chloride modification and polymer grafting.

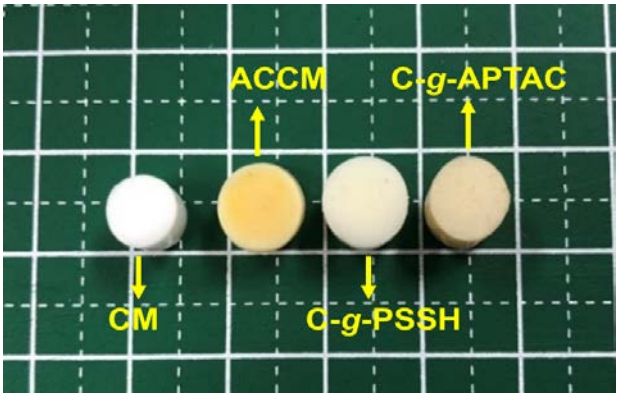

Figure 2-2. Digital photograph of CM, ACCM, C-*g*- PSS and C-*g*- APTAC monoliths.

With the purpose of verifying the successful preparation of ACCM, C-*g*-PSS and C-*g*-APTAC monoliths, FT-IR and elemental analysis characterization techniques were employed (see Figure 2-3). It can be found that the characteristic peak of CAM at and 1743 cm^{-1}, corresponding to the carbonyl groups, disappeared at the curve of CM. A newly appeared board peak centered at around 3400 cm^{-1} in the curve of CM, which was attributed to the hydroxide groups. Concerning the ACCM, compared with the reference sample, a new peak at around 1720 cm^{-1} assigned to C=O stretching vibration, confirmed

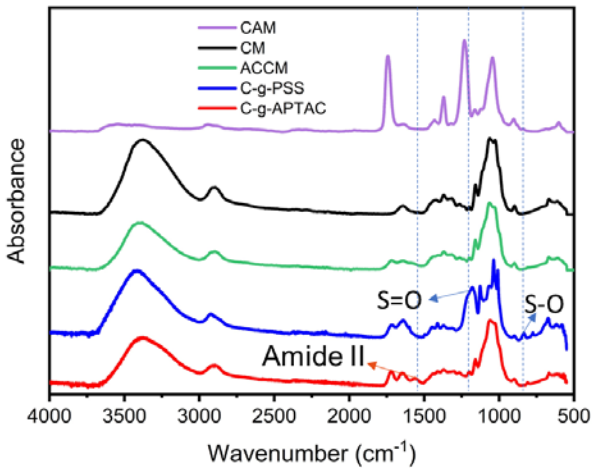

Figure 2-3. ATR-FTIR spectra of CAM, CM, ACCM, C-*g*-PSS and C-*g*-APTAC.

the introduction of acryloyl groups to the cellulose monolith. Distinctive absorption bands at around 1200 cm^{-1}, and 830 cm^{-1} appeared in the spectra of C-*g*-PSS monolith[10-11] and a new characteristic peak at around 1550 cm^{-1} appeared in the spectra of C-*g*-APTAC monolith,[12] corresponding to the characteristic bands, namely S=O stretching vibration, S-O bending vibration in sulfonic acid groups and amide II in amide groups, which confirmed the occurrence of the free-radical polymerization.

Moreover, elemental analysis reveals that there were 3.74 % sulfur by mass in the C-*g*-PSS and 1.18 % nitrogen by mass in the C-*g*-APTAC monolith (see Table 2-1). Calculated amount of the grafted PSS and APTAC are 0.55 g g^{-1} and 0.42 g g^{-1}, respectively. Successful polymerization further explains the reason for the change in pore size of C-*g*-PSS and C-*g*-APTAC monoliths. In addition, the results of the composition analyses for the CM, C-*g*-PSS and C-*g*-APTAC monoliths are summarized in Table 2-2.

Table 2-1. Elemental composition of monolith samples

Sample	Carbon (%)	Hydrogen (%)	Nitrogen (%)	Sulfur (%)
CM	40.7	6.30	-	-
C-*g*-PSS	42.8	5.65	-	3.74
C-*g*-APTAC	41.5	6.28	1.18	-

Table 2-2. Compositions of CM and modified monoliths

Sample	R_w (wt%)	R_c (wt%)	*PG* (wt%)
CM	85.8	14.2	0
C-*g*-PSS	87.2	8.4	4.4
C-*g*-APTAC	88.1	8.9	3.0

N_2 adsorption/desorption isotherm

The N_2 adsorption-desorption isotherms and pore size distribution (PSD) plots of the modified monoliths are displayed in Figure 2-4. All curves can be classified as type IV with adsorption hysteresis loops in terms of IUPAC classification. A pronounced hysteresis loop of type H1 was observed at high relative pressure ranging from 0.7 to 1 for the ACCM and 0.6 to 1 for the C-*g*-PSS monolith, the obviously steep tails at P/P_0=0.9 suggesting the predominance of mesopores (2-50 nm) and macropores (>50 nm). ACCM exhibited wider pore size distribution than either C-*g*-PSS or C-*g*-APTAC. The PSDs of the monoliths were investigated based on density functional theory (DFT). A sharp peak of around 4.9 nm was observed in both C-*g*-PSS and C-*g*-APTAC monoliths. This reveals that mesopores which are beneficial for the adsorption of macromolecules are dominant in both monoliths.

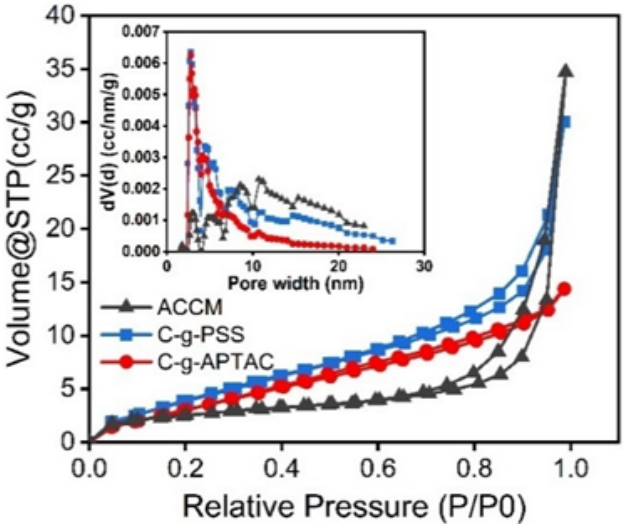

Figure 2-4. Nitrogen adsorption-desorption isotherms of ACCM, C-*g*-PSS and C-*g*-APTAC monoliths. Inset: pore size distribution plots by DFT method.

The BET surface areas, pore volumes and average pore diameters are shown in Table 2-3. The BET surface areas of ACCM drastically decreased compared with the

pristine CMs, indicates that some pores are closed during the acryloyl chloride modification processes, which strongly support the results of SEM analysis. After polymerization, the surface area of C-*g*-PSS and C-*g*-APTAC monoliths slightly increased to18.5 $m^2 g^{-1}$ and 15.8 $m^2 g^{-1}$, respectively. The decreased pore volume and pore size of C-*g*-PSS and C-*g*-APTAC, which are also key factors affecting the surface area, can be explained by introduction of polymers that some bigger voids in the monoliths are transformed to smaller ones. This may result in an increase in the number of active sites for the adsorption of dyes and sequentially affect the performance of the adsorbent.

Table 2-3. Porous parameters comparison of CM, C-*g*-PSS and C-*g*-APTAC monoliths.

Sample	Surface area ($m^2 g^{-1}$)	Total pore volume ($cm^3 g^{-1}$)	Average pore diameter (nm)
CM	101	0.33	13.0
ACCM	9.09	0.05	23.7
C-*g*-PSS	18.5	0.05	10.1
C-*g*-APTAC	15.8	0.02	5.63

Evaluation of permeability

The monolith permeability coefficient in the flow system, B_0, was calculated by taking the average measurements of pressure loss at a flow rate of 1, 2 and 3 mL min^{-1}, in that order. The average of the three measurements of the pressure loss was also analyzed to determine ways of reducing deviation caused by backpressure fluctuations. Looking at the data presented in Table 2-4, it is clear that as the flow rate increases across the monolith, so does the pressure drop. After increasing the flow rate from 1 to 3 mL min^{-1}, the pressure drop values were recorded as 3.5-10.3 kPa for the CM, 1.1-3.2 kPa for the C-*g*-PSS monolith and 1.0-3.1 kPa for the C-*g*-APTAC monolith. The pressure drop is

proportional to the runoff of the liquid passing through the monolith. Permeability is higher in the ion exchange monoliths than in the unmodified ones. The increase in permeability after modification is brought about by the increase in pore size. The high permeability of the modified monoliths is highly effective and viable for flow-through applications.

Table 2-4. Permeability comparison of CM, C-*g*-PSS and C-*g*-APTAC monoliths.

q (mL min^{-1})	v (cm s^{-1})	Pressure drop ΔP (kPa)	Permeability* B_0 (D)
CM			
1	0.059	3.5	0.91
2	0.118	6.7	0.94
3	0.177	10.3	0.92
C-*g*-PSS			
1	0.043	1.1	2.10
2	0.087	2.2	2.14
3	0.130	3.2	2.20
C-*g*-APTAC			
1	0.043	1.0	2.24
2	0.087	2.0	2.31
3	0.130	3.1	2.26

*Permeability is calculated at L=6 mm, i.d.=7 mm (for C-*g*-PSS and C-*g*-APTAC), and i.d=6 mm (for CM) by pressure drop obtained from average of 3 measurements.

Dynamic adsorption by continuous flow system and monolith regeneration studies

To investigate the dye adsorption behaviors, CM was firstly used to adsorb acid red 70 and methylene blue dyes in the continuous flow system. Author found that only small amount of dyes can be adsorbed on CM and will be completely eluted by water because CM are nonionic polymers. Eluted methylene blue and acid red 70 dyes were

only 0.02 mg g^{-1} and 0.01 mg g^{-1}, respectively, which can be neglected in analyzing ionic exchange manner of modified CM.

Effect of initial concentration

The effect of initial inlet concentration on the adsorption onto monoliths was examined at a flow rate of 1 mL min^{-1} with the monolith length of 7 mm at ambient temperature. The results are shown in Figure 2-5 a, b and have been summarized in Table 2-5. As can be seen from the plots, a similar scenario is observed for both C-*g*-PSS and C-*g*-APTAC monoliths adsorption assays. The equilibrium time and the breakthrough time both decreased with increase in the initial dye concentration. The breakthrough happened faster with higher concentration since a higher concentration gradient leads to fast transport of dyes to the surface of the adsorbent due to the increase of both the diffusion coefficient and the mass transfer driving force. The highest efficiency of methylene blue removal was 72.3 % and an adsorption capacity of 606 mg g^{-1} was observed at the lowest inlet dye solution concentration of 300 ppm for C-*g*-PSS monolith adsorption assay. The reason for this is that there will be empty active sites on the adsorbent surface at low concentration, and no active sites required for adsorption will be present when the initial dye concentration increases. The efficiency of the removal of acid red 70 in the C-*g*-APTAC monolith decreased from 67.2 % to 57.5 % when the initial feed solution concentration was increased from 75 ppm to 200 ppm. Meanwhile, the adsorption capacity increased from 52.8 mg g^{-1} to 58.6 mg g^{-1}. This was brought about by an increase in the total amount of dye solution passed through the monolith, which provides a higher driving force for the transfer process to prevail over the mass transfer resistance until the adsorption sites are fully saturated. Hence, the diffusion process can be regarded as concentration dependent.

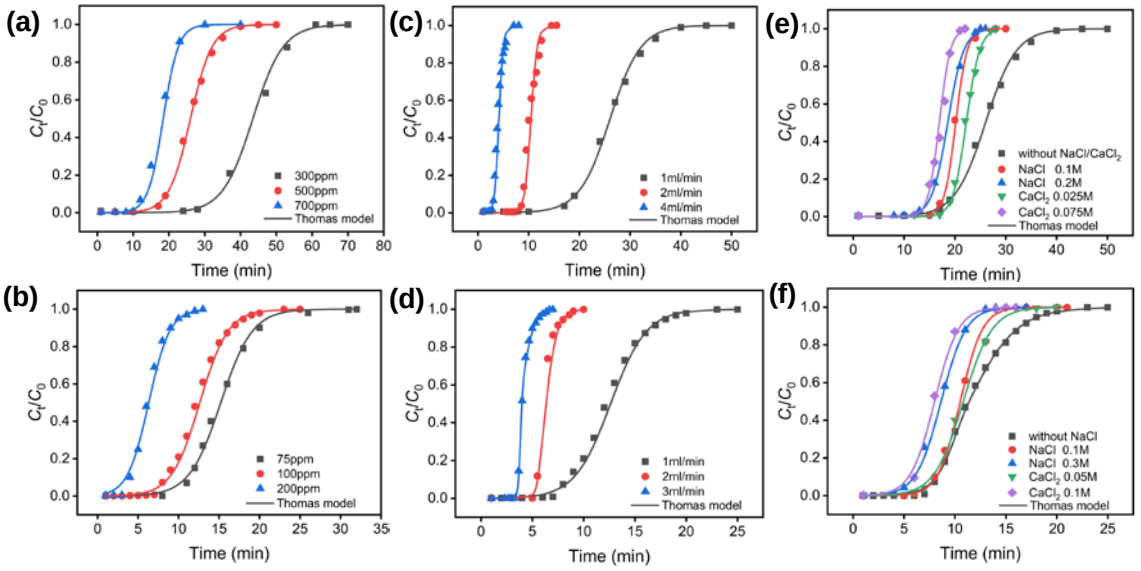

Figure 2-5. Experimental and predicted breakthrough curves of methylene blue adsorption by C-*g*-PSS monolith (a, c and e); acid red 70 adsorption by C-*g*-APTAC monolith (b, d and f) predicted by the Thomas model; **(a, b)** at different initial concentration (flow rate=1 mL min^{-1}, L=7 mm); **(c, d)** at different flow rates (Acid red 70, C_0=100 ppm; methylene blue, C_0=500 ppm, L=7 mm); **(e, f)** at different ionic strength (Acid red 70, C_0=100 ppm; methylene blue, C_0=500 ppm, flow rate=1 mL min^{-1}, L= 7 mm). Inset: molecular structure of reactive dyes.

Effect of flow rate

To determine the optimum flow rate for dye adsorption on monoliths, different flow rates through monoliths of 7 mm in length were tested. All the parameters are shown in Figure 2-5 c, d and summarized in Table 2-5. Acid red 70 with an influent concentration of 100 ppm and methylene blue with an influent concentration of 500 ppm were used for the adsorption assays of C-*g*-APTAC and C-*g*-PSS monoliths, respectively. The breakthrough curves of both groups of the adsorption experiments show a reduction of time to arrive at both the breakthrough point and equilibrium with increasing of flow rates. The efficiency of the dye removal tends to increase at first and then decrease with increase of the flow rate. For the C-*g*-APTAC monolith, the highest total dye removal and

experimental adsorption capacity were obtained at the flow rate of 2 mL min^{-1}. This may be explained by the fact that the mass transfer rate tends to increase as the flow rate increases, which leads to an increase in the amount of dye adsorbed onto the unit monolith length. Ultrafast adsorption capacity improves the efficiency of dye removal efficiency and also increases the influent flow rate. However, further increase of the flow rate will lead to faster saturation, which will significantly reduce the active life of the monolith. Conversely, for the C-*g*-PSS monolith, the highest experimental adsorption capacity was obtained at the lowest flow rate of 1 mL min^{-1}, possibly because the time the dye solution stayed in the monolith was enough for the adsorption to reach equilibrium. It is worthy considering that a significant increase of the influent flow rate can improve the efficiency of the dye removal in practical applications.

Table 2-5. Experimental data and parameters obtained at different operating conditions

	C_0 (mg L^{-1})	Q (mL min^{-1})	t_b (min)	t_e (min)	q_e (mg g^{-1})	q_u (mg g^{-1})	M_t (mg)	*Removal* (%)
Acid red 70	100	1	8.9	17.7	58.3	43.5	1.77	65.9
(C-*g*-APTAC)	100	2	5.6	8.0	60.3	56.0	1.59	75.7
	100	3	3.7	5.6	58.5	55.6	1.68	69.6
	75	1	11.0	20.9	52.8	40.6	1.57	67.2
	200	1	3.5	10.0	58.6	33.9	2.00	57.5
Methylene blue	500	1	19.5	34.9	603	478	17.5	69.4
(C-*g*-PSS)	500	2	9.1	12.2	490	453	12.2	80.1
	500	4	3.2	5.4	384	318	10.7	71.5
	300	1	34.2	55.9	606	507	16.8	72.3
	700	1	14.0	24.6	598	481	17.5	68.3

Effect of ionic strength

Dye wastewater, especially from the textile industry, often contains high levels of solute salts. Therefore, the effect of ionic strength on adsorption is necessary for a proper assessment of the adsorption process. The ionic strength of dye solutions was adjusted by altering the concentration of sodium chloride or calcium chloride. As can be seen in Figure 2-5 e, f for the adsorption of acid red 70 on C-*g*-APTAC and the adsorption of methylene blue on the C-*g*-PSS, both breakthrough and equilibrium time reduced with the increase of ionic strength. For the C-*g*-APTAC, this situation may be interpreted as being caused by the reduction of the positive charge on the surface bringing about lower attraction of anions. Furthermore, Cl^- ions may compete with the anionic dye for binding

Table 2-6. Experimental data and parameters obtained at different ionic strength conditions.

		t_b (min)	t_e (min)	q_e (mg g^{-1})	q_u (mg g^{-1})	M_t (mg)	*Removal* (%)
Acid red 70	None	8.9	17.7	58.3	43.5	1.77	65.9
	NaCl 0.1M	8.3	13.6	49.0	40.7	1.36	72.0
	NaCl 0.3M	6.1	12.1	39.9	29.8	1.21	65.9
	CaCl2 0.05M	7.8	14.9	50.0	38.1	1.49	67.2
	CaCl2 0.1M	5.5	11.4	36.9	26.8	1.14	64.6
Methylene blue	None	19.5	34.9	603	478	17.5	69.0
	NaCl 0.1M	17.8	23.4	474	442	11.7	80.9
	NaCl 0.2M	13.3	23.1	434	331	11.6	75.1
	CaCl2 0.025M	19.4	25.9	522	472	13.0	80.5
	CaCl2 0.075M	14.6	20.0	397	362	10.0	79.4

sites on the monolith surface and this will negatively affect the electrostatic attraction between quaternary amine group and the dye. Moreover, the efficiency of dye removal increased upon addition of small quantities of salt, as shown in Table 2-6, this phenomenon happens on both adsorbents. However, further increase in salt concentration will lead to a decrease in efficiency. The increase in dye removal after a moderate increase in ionic strength can be attributed to an increase in the dimerization of reactive dyes in the solution. A number of intermolecular forces have been suggested to explain this aggregation. These forces include van der Waals forces, ion-dipole forces, and dipole-dipole forces, which act between dye molecules in the solution. In general, an increase in ionic strength will lead an increase in the removal efficiency for both adsorbents, while faster saturation makes a rapid arrival on the breakthrough point and thus limit the total adsorption amount.

Modelling of the Breakthrough Curves

The Thomas Model

As can be seen in Table 2-7, the value of q_e increased and the value of K_{Th} decreased with an increase in the initial dye concentration. The maximum adsorption capacity q_e and K_{Th} first increased and then started decreasing as the flow rate increased. It can thus be concluded that a lower flow rate and a higher initial concentration leads to better adsorption performance. From Figure 2-5, it can be observed that the experiment values and the predicted values obtained from the Thomas model are almost similar for all the experimental conditions. The regression coefficient for the adsorption of acid red 70 is higher than 0.9626, while that of methylene blue is higher than 0.9689. These values are testament to the validity of the model for all conditions, which is an indication that the model performs well in its prediction of the adsorption process. This model is largely

the most appropriate method for describing processes in which the flow rate is not affected by internal diffusion.

Table 2-7. The Thomas model parameters obtained at different experimental conditions.

	C_0 (mg L^{-1})	Q (mL min^{-1})	K_{Th} (mL min^{-1} mg^{-1})	q_e' th (mg g^{-1})	q_e' exp (mg g^{-1})	R^2
Acid red 70						
	100	1	5.9	60.8	58.3	0.9697
	100	2	17.7	62.7	60.3	0.9626
	100	3	16.7	59.7	58.5	0.9881
	75	1	7.0	54.3	52.8	0.9771
	200	1	4.0	61.6	58.6	0.9905
Methylene blue						
	500	1	0.67	616	603	0.9903
	500	2	3.42	496	490	0.9737
	500	4	4.82	393	384	0.9696
	300	1	0.79	621	606	0.9689
	700	1	0.69	610	598	0.9757

Desorption and recyclability

The effective stability and regeneration ability of the adsorbents are essential standards for practical applications. Therefore, research on the reusability of the adsorbent is highly important. Fast and efficient desorption experiments for the regeneration of the C-*g*-APTAC monolith were carried out using the mixtures of ethanol, sodium chloride and water desorption agent. The mixtures of hydrochloric acid and 1-butanol desorption agent were used to regenerate the C-*g*-PSS monolith.[13] After each desorption process, the monolith was thoroughly washed with DI water before next adsorption-desorption cycle. The adsorption of acid red 70 with an initial concentration of 100 ppm at a flow rate of

1mL min^{-1}, and the adsorption of methylene blue with initial concentration of 500 ppm at the flow rate of 1mL min^{-1} were selected for the recyclability analysis. In the elution process, for the C-*g*-APTAC monolith, almost all the adsorbed dyes could be desorbed at flow rate of 3 mL min^{-1} within 10 min. The recyclability of C-*g*-APTAC and C-*g*-PSS monoliths was investigated by repeating the adsorption-desorption process seven times. The adsorption efficiency of the first cycle was considered to be 100 %. For the C-*g*-APTAC monolith, the adsorption efficiency hardly changed for the first five cycles. The adsorption ratio was still very high even at the seventh adsorption cycle. Regarding the C-*g*-PSS monolith, the reduction of the adsorption efficiency was obvious. After seven successive cycles, the adsorption efficiency dropped by 31 % (See Figure 2-6). The obtained data clearly demonstrate that the C-*g*-APTAC monolith has a better and efficient regeneration capability even after multiple usage.

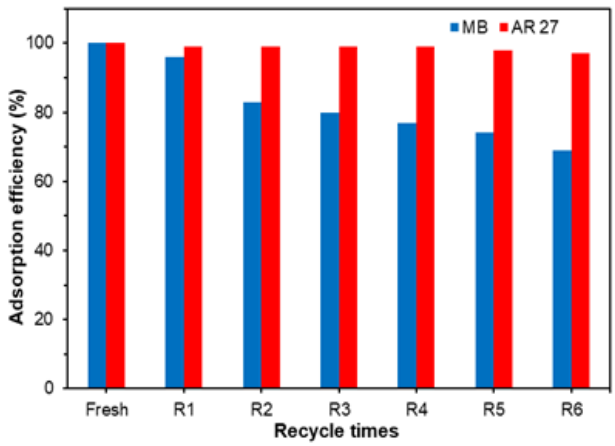

Figure 2-6. Regeneration test of C-*g*-APTAC and C-*g*-PSS monoliths for 7 cycles. (Aqueous dye solution without ionic strength adjustment; acid red 70: C_0=100 ppm; methylene blue: C_0=500 ppm, desorption flow rate=2 mL min^{-1}, desorption time:10 min).

2.4 Conclusion

In this study, cation and anion exchange monoliths were prepared by the

modification of cellulose with a simple radical polymerization of anionic and cationic monomers, respectively. These modified monoliths have been proved to successfully remove anionic or cationic dyes from water and high dye recoveries were achieved using appropriate desorption conditions. Both kinds of the ion exchange monoliths have the benefit of saving energy as well as the reactive dye removal-time. It was found that C-*g*-PSS monolith exhibited greater adsorption capacity and removal efficiency and could bind with the cationic dyes more quickly and strongly compared with the C-*g*-APTAC monolith. However, the C-*g*-APTAC monolith achieved better dye recovery and regeneration ability. Moreover, the dye removal process took no more than 1 h to complete the adsorption and desorption cycle under a negligible pressure drop. Other advantages include the low cost and scale-up design can be easily realized by enlarging the monolith. A concept of monolith preparation and its flow-based operation are applicable to not only dyes adsorption but also heavy metal ion adsorption or bioseparation. Author believes these monoliths will also show excellent performance.

2.5 References

1. Robinson T, Mcmullan G, Marchant, *Bioresour Technol*. 2001, **77**, 247-255.
2. Pinheiro H M, Touraud E, Thomas O, *Dyes & Pigments*, 2004, **61**, 121-139.
3. Karcher S, Kornmu A, Jekel M, *Dyes Pigm*, 2001, **51**, 111-125.
4. Ahmad A A, Hameed B H, *J. Hazard. Mater*, 2010, **175**, 298-303.
5. Bayramoglu G, Altintas B, Arica M Y, *Chem Eng J*, 2009, **152**, 339-346.
6. Wang C, Juang L, Lee C, *J Colloid Interface Sci*, 2004, **280**, 27-35.
7. Tahir S S, Rauf N, *Chemosphere*, 2006, **63**, 1842-1848.
8. Rafatullah M, Sulaiman O, Hashim R, *J Hazard Mater*, 2010, **177**, 70-80.

9. He X Y, Male K B, Nesterenko P N, *ACS Appl Mater Interfaces*, 2013, **5**, 8796-8804.

10. Li D, Mao D, Li J, *Applied Catal. A*, 2016, **510**, 125-133.

11. Manoilova O V, Olindo R, Carlos O A, *Catal Commun*, 2007, **8**, 865-870.

12. Kumar K, Adhikary P, Karmakar N C, *Carbohydr Polym*, 2015, **127**, 275-281.

13. Daneshvar E, Vazirzadeh A, Niazi A, *J Clean. Prod*, 2017, **152**, 443-453.

Chapter 3.

Cellulose Monoliths Supported Metal/Organic Framework as Hierarchical Porous Materials for Flow Reaction

3.1 Introduction

Flow-based techniques allow the establishment of automated analysis methods and prompt analytical enrichment.[1,2] Some researchers have tried to examine the use of flow-through MOFs-based composite materials to scale down and automate heterogeneous catalysis processes. Their efforts have made possible the reproducible preconcentration of environmental pollutants, as well as the rapid purification of biomolecules or high-performance liquid chromatography.[3] It is perceived that suitable flow-through supports and proper surface modification are vital for the deposition of MOF layers having high structural quality and low defect density, since they have an obvious influence on the feasibility and effectiveness of flow-based applications. Typical synthetic strategies usually embed MOF crystals directly in a polymer or in situ MOF synthesis on a functional support. These strategies make it hard to regulate the growth of coating, leading to the creation of non-homogeneous MOF layers. Moreover, the majority crystals within the polymer scaffold will affect efficiency owing to the inactivation of some MOFs in certain applications. [4-5] Another advanced strategy is the layer-by-layer (LbL) approach based on liquid phase epitaxy, which allows for accurate control over the growth of a uniform MOF coating. However, this method is tedious and time-consuming, and only works when incorporating the MOF onto planar substrates or the surface of

particles. Nonetheless, the incorporation of MOF on the surface of the internal skeleton of polymer materials is quite beneficial for a majority of applications requiring flow-through support.

To resolve these anomalies, author is proposing a quick and highly effective automated pump injection approach for the controlled growth of MOF coatings on pores of polyelectrolyte modified cellulose monolith. The additional nanoparticle architectures introduced by the MOF layer is thought to be beneficial for flow-based applications owing to the improved chemical and mechanical stability. ZIF-8, a subclass of MOFs, was selected as a prototype material for this strategy mainly because of its reproducible straightforward synthesis and intrinsic microporosity.[6,7] The exact value of the synthesized ordered macro-microporous ZIF-8-coated conjugate monolith is examined by heterogeneous catalysis, and the extraction and preconcentration of trace levels of environmental pollutants from water.

3.2 Experimental section

Chemicals and materials

Zinc nitrate dexahydrate ($Zn(NO_3)_2 \cdot 6H_2O$) ($\geq$ 99.0%) was purchased from Wako Chemicals (Osaka, Japan). 2-methylimidazole (HMIM) ($\geq$ 99.0%) was provided by TCI, Ltd. (Tokyo, Japan). The other organic solvents were offered by graduate school of engineering, Osaka University. All chemicals and reagents were of analytical grade and used without further purification.

Synthesis of C-g-PSS monolith supports

C-*g*-PSS monolith was obtained via free-radical polymerization by treatment of acryloyl group-introduced cellulose monolith with sodium *p*-styrene sulfonate in the

presence of ammonium persulfate initiator to acquire suitable anchoring sites for the growth of ZIF-8. Details have been described in chapter 2.

Preparation of ZIF-8 precursor and bulk ZIF-8

The ZIF-8 crystals precursor was prepared by mixing methanolic 2-methylimidazole (HmIm) and $Zn(NO_3)_2 \cdot 6H_2O$ methanolic solutions in plastic vials and stirred for 20 min at room temperature as reported in other literature.[8] It has been mentioned earlier that the structure and performance of the ZIF-8 crystals can be greatly influenced by the reactant concentration.[9] Thus, the nucleation effect of different ZIF-8 reactant concentration on sulfonate-decorated monolith was discussed in this work. When the concentration of ZIF-8 was measured, the obtained samples were referred to as ZIF-8-*n*c (*n*=1, 2, 3 and 4) as shown in Table 3-1. ZIF-8-2c had a similar concentration to that reported by Rafti M.[10] The bulk ZIF-8 was obtained by transferring the reaction mixture to a tightly capped vessel and heating it in a programmable oven at a rate of 5 °C to 100 °C, and maintaining this temperature for 5 h before cooling to room temperature. The obtained white crystals were collected by centrifugation, thoroughly washed with methanol, and dried at room temperature.

Table 3-1. ZIF-8 reactant concentrations

ZIF-8	HMIM concentration in methanol (g L^{-1})	$Zn(NO_3)_2 \cdot 6H_2O$ concentration in methanol (g L^{-1})
ZIF-8-1c	2.3	3.7
ZIF-8-2c	4.6	7.4
ZIF-8-3c	9.2	14.8
ZIF-8-4c	23.0	37.0

Synthesis of ZIF-8@PSS monoliths

ZIF-8@PSS monoliths were prepared by coating the PSS functionalized CM with a thin layer of ZIF-8 MOF using a pump injection method. Firstly, the sulfonate-decorated monolith was tightly fitted into a heat shrink tubing and connected to a digital quantitative tubing pump (DSP-100SA, As One, Japan) and a ZIF-8 precursor vessel circulatory system by polypropylene tubing. This was done to ensure a constant controllable flow rate. The reaction was left to proceed at room temperature for appropriate time to allow for ZIF-8 growth. Finally, the monolith was copiously washed with methanol. The pump injection time and flow rate of ZIF-8 precursor were analyzed. When *x* of reaction time had passed, the obtained samples were referred to as ZIF-8-*x*t (*x*=10, 20, 30 and 40 min), and when m of ZIF-8 flow rate was performed, the obtained samples were referred to as ZIF-8-*m*f (*m*= 0.2, 0.5, 1 and 1.5 mL min^{-1}). The details of the fabrication of ZIF-8 layers on the C-*g*-PSS monolith are summarized in Scheme 3-1.

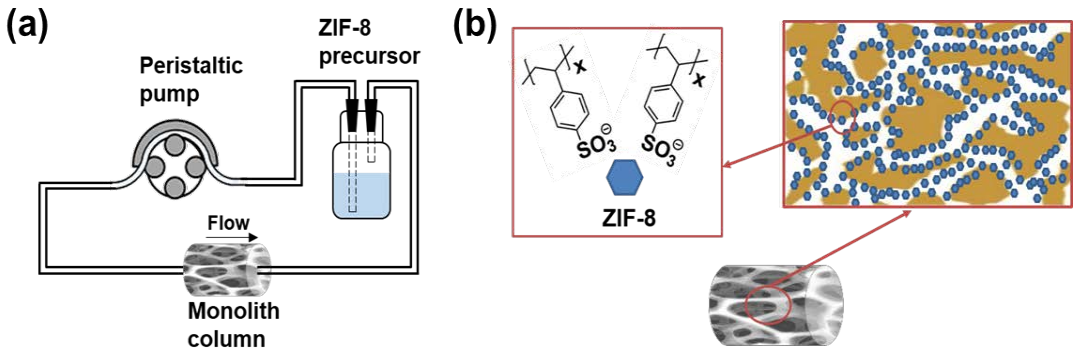

Scheme 3-1. (a) Schematic diagram of pump injection system assays for preparing ZIF-8@PSS monolith; **(b)** schematic representation of the fabrication of ZIF-8 layers on C-*g*-PSS monolith.

Characterization

The morphologies of all samples were analyzed by scanning electron microscopy (Hitachi SU3500, Japan) with an accelerating voltage of 10kV. The surface chemical

composition of ZIF-8@PSS monolith was determined using X-ray photoelectron spectroscopy (XPS). The XPS spectra was recorded using a Kratos Ultra 2 spectrometer employing a monochromatic Aluminum Kα X-ray source. The survey and high-resolution XPS spectra were collected at fixed analyzer pass energies of 160 eV and 10 eV, respectively. Inductively coupled plasma atomic emission spectroscopy (ICP-AES) (Shimadzu Sequential Plasma Emission Spectrometer ICPS-7510) were used to confirm the successful coating of ZIF-8. Nitrogen adsorption/desorption isotherms were measured at 77K using a NOVA 4200e surface area & pore size analyzer (Quantachrome Instruments). Before measurements, the sample was degassed at room temperature under vacuum for at least 6 h. The specific surface area was calculated based on the Brunauer-Emmett-Teller (BET) model. The monoliths' mechanical response towards compressive stress were recorded on a table-top material tester (Shimadzu EZ Graph, Japan) at room temperature using a 500 N load cell at 5 mm min^{-1} compression rate. Samples were measured in triplicates and their elastic modulus was determined from the initial linear slope obtained from the stress−strain plot. The stress at yield was recorded to show monoliths compression strength. High-performance liquid chromatography (HPLC) was used for quantification of the water pollutants in extraction experiments and for following the conversion process in the catalytic reaction.

Catalytic experiment

The flow-through catalytic experiments were carried out following a procedure reported in the literature with some changes.[11] The monolith was first thoroughly washed with copious amount of ethanol. The mixture of reactant composed of 2.2 mL benzaldehyde, 2.3 mL ethyl cyanoacetate, and 1.5 mL dimethyl sulfoxide was conducted in a glass vial with a rubber plug and pumped through the monolith at a desired flow rate.

The eluent was collected back to the glass vial. The monolith microreactor was deployed in a water bath at 70 ℃. The mixture in the glass vial was periodically monitored by HPLC. The benzaldehyde conversion and product yield were calculated. The batch reactions of ZIF-8 catalysis and ZIF-8@PSS monolith was carried out in a round-bottom glass flask with mechanically stirring under similar condition.

Preconcentration of micropollutants

The procedure was automated using a sequential pump injection analysis (SPIA), this system is referred to previous publication with minor changes. The SPIA system comprised a bi-directional quantitative tubing pump (DSP-100SA, As One, Japan) equipped with a selection valve 1. All joint tubing was made of polytetrafluoroethylene (PTFE) 0.8 mm I.D. A desired sample volume was loaded through selection valve 1 and pumped through the monolith column, followed by a volume of carrier to wash the non-retained analytes in the monolith. And the outlet of the monolith is connected to a waste reservoir through the selection valve 2. Thereafter, loading appropriate amount of eluent through selection valve 1, and then collecting the eluent fraction in a vial for subsequent HPLC analysis of the extracted analytes. The collected solvent was evaporated under a gentle stream of nitrogen and reconstituted in 50 μL of acetonitrile. A 20 μL portion was used for HPLC analysis (Scheme 3-2).

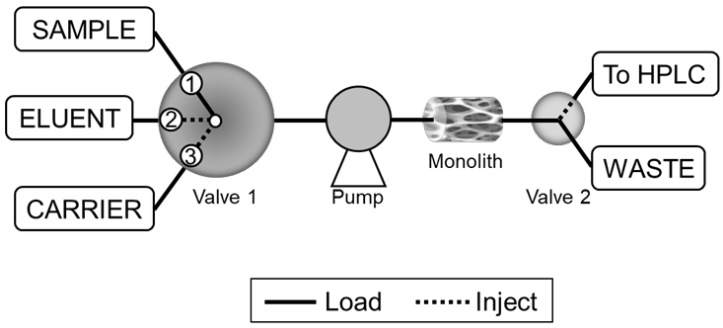

Scheme 3-2. Schematic diagram of SPIA system

3.3 Results and discussion

Morphology and composition of monolith

In preliminary experiments, we prepared ZIF-8@PSS monoliths using the LbL method reported in other literatures.[10] This was done to explore the effect of reactant concentration on the performance of ZIF-8 layer coated on the sulfonate-modified monolith and then optimize it for flow-based applications. The SEM images revealed the surface morphology of ZIF-8@PSS monoliths corresponding to different reactant concentrations. Firstly, author followed a similar reactant concentration proposed in other literature, as shown in Figure 3-1 b (c(HMIM)=4.6 g L^{-1}, c (zinc salt) =7.4 g L^{-1}; ZIF-8-2c@PSS). It can be seen that the ZIF-8 layer obtained can form a tightly-intergrown layer. When the concentration of reactants was halved (ZIF-8-1c@PSS), the ZIF-8 crystals on the monolith's surface formed a more compact layer with smaller crystals size as illustrated in Figure 3-1 a. When the concentration of reactants was doubled (ZIF-8-3c@PSS), the SEM image (Figure 3-1 c) showed a superior ZIF-8 crystal layer with relatively larger rhombic dodecahedron morphology. However, a further increase in reactant concentration (c(HMIM)=20.6 g L^{-1}, c (zinc salt)=37.2 g L^{-1}; ZIF-8-4c@PSS) produced a poorly intergrown crystal layer with insufficient density. In this case, the ZIF-8 coating is predominantly formed by sub-micrometric crystals, although some much larger crystals are present within the layer structure. It can thus be concluded that crystal growth depends on the level of reactant concentration. In general, crystal size decreases with metal and ligand concentrations. To achieve a larger specific surface area and a more homogeneous ZIF-8 layer, ZIF-8-1c precursor was selected for further studies.

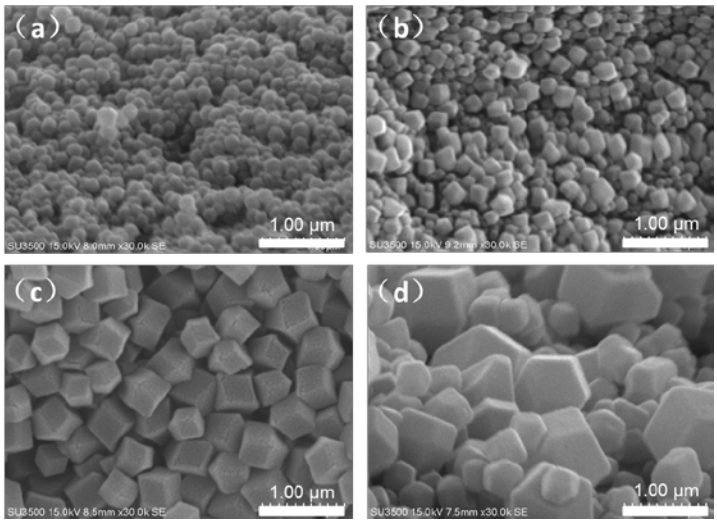

Figure 3-1. SEM surface images of ZIF-8@PSS prepared by LbL method with different reactant concentrations: a) ZIF-8-1c@PSS, b) -2c, c) -3c, and d) -4c.

Further examination of cross-sectional micrographs through pump injection experiments showed that there were noticeable morphological differences between C-*g*-PSS and ZIF-8@PSS monoliths (Figure 3-2). It was observed that the C-*g*-PSS monolith had a continuous three-dimensional porous network made up of highly cross-linked clusters that are aggregated and assembled into an interconnected structure. This type of morphology is similar to that of the bare cellulose monolith. When the pump injection method was used, the ZIF-8 crystals were uniformly and compactly coated on the surface and internal skeleton of the monolith without causing any damage to the network. The aggregated and well-shaped crystals constituting the ZIF-8 layers had an average size of approximately 100-200 nm, which made the monolith skeleton to have a bigger diameter. The C-*g*-PSS monolith modified by free radical polymerization allowed a large number of anionic sulfonate moieties to be exposed to the contact interface. The great capacity of anionic sulfonate for uptake and exchange of Zn^{2+} cations led to the nucleation, deposition and growth of ZIF-8 on the internal skeleton. Once the ZIF-8 layer had grown, subsequent sequential crystallization growth of MOF multilayers was

triggered by flow-based ZIF-8 precursor during a preset growth time. While cellulose monolith itself doesn't have functional sites to anchor ZIF-8 nanoparticles, as shown in Figure 3-3. For the comparative experiment, pristine cellulose monolith was also used for the adsorption of ZIF-8 by the same pump injection method and was analyzed by FT-IR. Bigger size of ZIF-8 particles can be intercepted by the porous structure of CM, and some are stored in the pores present in the monolith. However, it can't be immobilized on the cellulose support, and will be totally washed with methanol from unmodified cellulose monolith.

Pump injection strategy was implemented in previous LbL synthesis as homogeneous and heterogeneous nucleation processes occur simultaneously, and the coating thickness can be controlled by adjusting the pump injection time or flow rate. Compared with LbL methods, flow-based strategy implemented on anionic polyelectrolyte modified monolith allows for the homogeneous nucleation and deposition of ZIF-8 propulsion, which achieves thick highly crystalline layers at high deposition rates in a rather controllable manner.

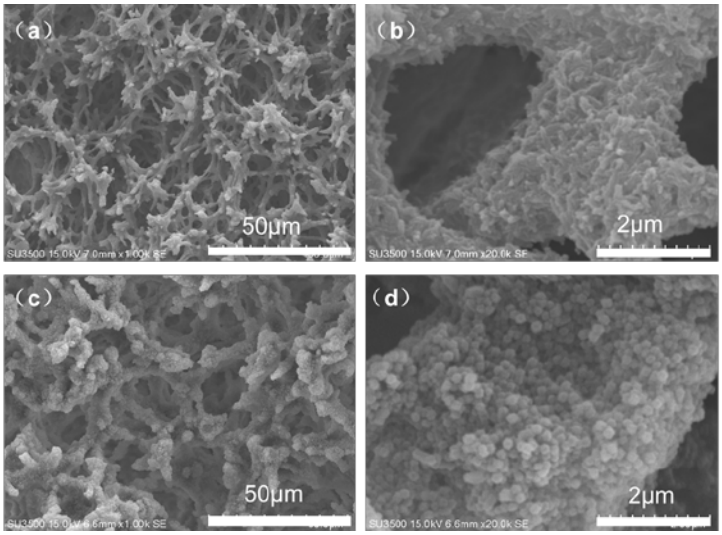

Figure 3-2. Cross-sectional images of (a, b) C-*g*-PSS monolith; (c, d) ZIF-8@PSS monolith prepared by flow-based method at flow rate of 1mL min^{-1} for 30 min.

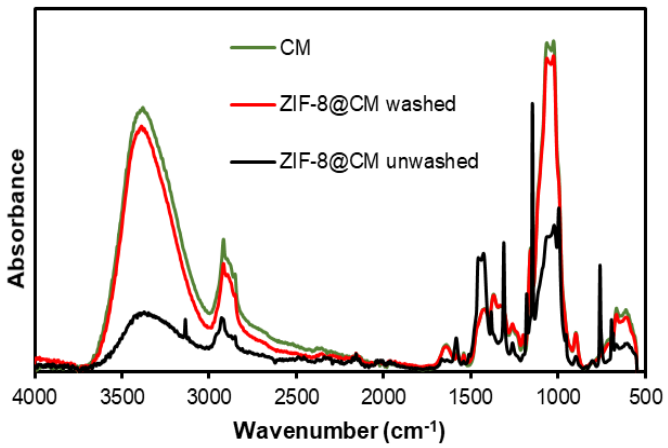

Figure 3-3. FT-IR spectra of CM, ZIF-8@CM monoliths washed with methanol and without washing.

Further, an XPS experiment was conducted to demonstrate the ability of the C-*g*-PSS monolith to coordinate the Zn^{2+} ions present in the flow-based ZIF-8 precursor solution. High resolution characterization confirmed the presence of Zn^{2+} ions in the ZIF-8@PSS monolith after pumping the ZIF-8 precursor solution into the as-synthesized, Na^{+}-coordinated C-*g*-PSS monolith for 30 min at a flow rate of 1 mL min^{-1} (Figure 3-4).

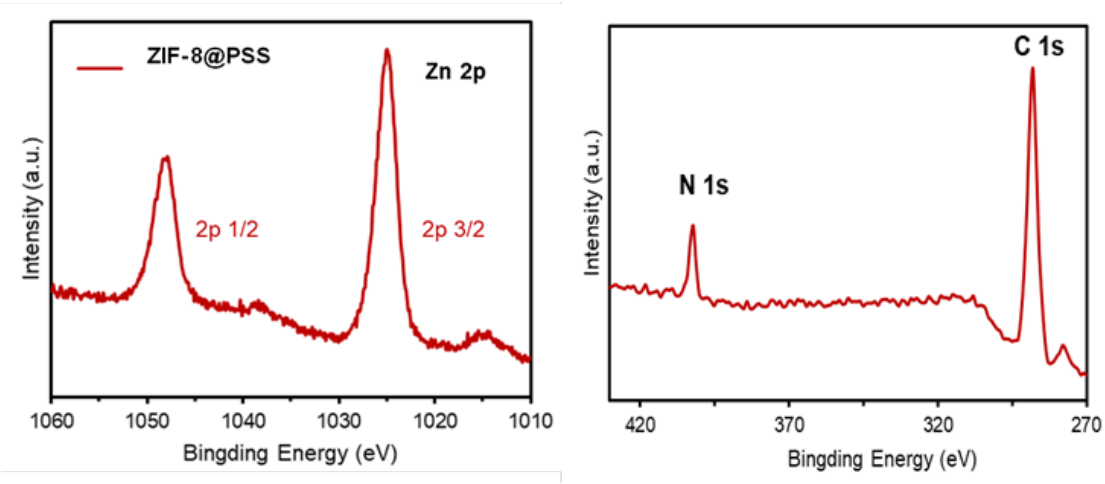

Figure 3-4. XPS spectra of a ZIF-8@PSS monolith. The binding energies of the Zn 2p3/2 and 2p1/2 peaks are 1021 eV and 1044 eV, respectively.

It can be observed that the values founded for C 1s, Zn 2p and N 1s are similar to previously reported XPS binding energies peak for ZIF-8.[10] This indicates that, in the presence of Zn^{2+} ion-rich solutions, ion exchange occurs at a certain flow rate. This means that Na^{+} ions are removed from the macromolecular environment of the C-*g*-PSS monolith and subsequently replaced by Zn^{2+} ions.

N_2 adsorption/desorption isotherm

Figure 3-5 illustrates textural characterization by means of nitrogen adsorption-desorption isotherms. The C-*g*-PSS monolith was predominantly mesoporous (2-50 nm) and macroporous (>50 nm), showing properties of a type IV isotherm with a pronounced hysteresis loop of type H3 in terms of IUPAC classification of isotherms. It also exhibited a low surface area and wider pore size distribution. Coating with ZIF-8 layer showed properties of a type I isotherm, and the drastic increase in the volume adsorbed at very low relative pressures is due to the presence of micropores. This was also confirmed by the pore size distribution with an average pore size of 2.4 nm based on the Density Functional Theory (DFT) method, which indicates that the porosity of the composite is mainly attributed to the ZIF-8 component. The growth of ZIF-8 layers also led to a dramatic increase in the BET surface area of ZIF-8-0.2f@PSS and ZIF-8-1f@PSS monoliths up to 228.4 m^2 g^{-1} and 262 m^2 g^{-1}, respectively, as shown in Table 3-2. The increment of the surface area is due to the deposition and growth of ZIF-8 on the surface of the monolith skeleton, which results in an increase of the total pore volume. Obviously, during the same pump injection time, the specific surface area of the monoliths can be adjusted by the flow rate and positively correlated with it.

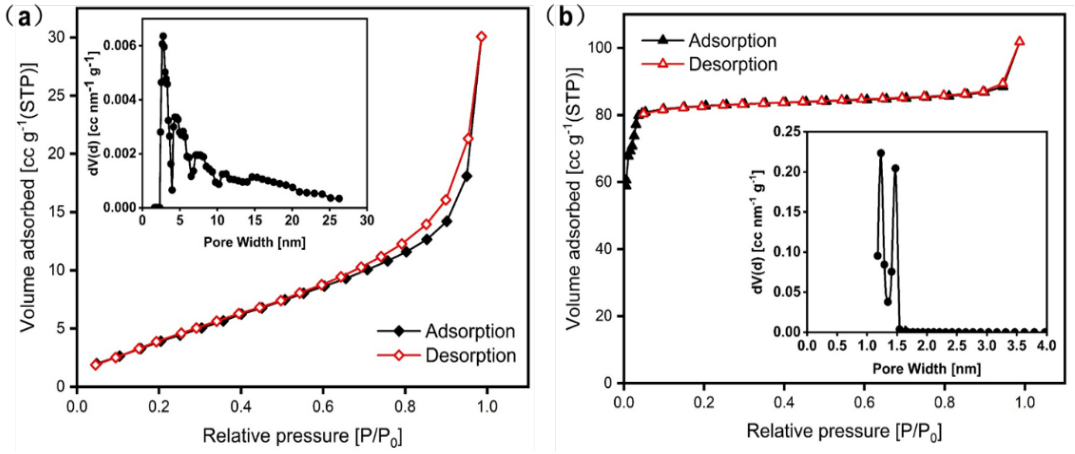

Figure 3-5. Nitrogen adsorption/desorption isotherms of (a) C-*g*-PSS monolith and (b) ZIF-8@PSS monolith (preparation time: 30 min; flow rate: 1 mL min^{-1}). Inset: pore size distribution plots.

Table 3-2. Porous parameters comparison of C-*g*-PSS and ZIF-8@PSS monolith prepared by pump injection method (pump injection: 30 min).

Sample	Surface area ($m^2 g^{-1}$)	Total pore volume ($cm^3 g^{-1}$)	Average pore diameter (nm)
C-*g*-PSS	18.5	0.05	10.06
ZIF-8-1f@PSS	261.9	0.16	2.41
ZIF-8-0.2f@PSS	228.4	0.15	2.56

Effect of pump injection time and flow rate

Author further performed experiments to assess the influence of pump injection time and flow rate on the binding amount of the ZIF-8 nanoparticles on the signal formation in single particle inductively coupled plasma mass spectrometry (spICP-MS) measurements by using dispersions containing Zinc nanoparticles. Here, the dried ZIF-8@PSS monolith (15 mg), completely dissolved in aqua regia, was prepared for testing. The results showed that the content of zinc in the monolith is positively correlated with both the pump injection time and flow rate. This implies that at the same flow rate,

the longer the injection time, the higher the amount of ZIF-8 nanoparticles in the coating. Then, at the same injection time, the zinc content increases with an increase of the flow rate. In other words, the preparation time can be decreased by increasing the injection flow rate. It is the sufficiently exposed sulfonate groups that give the zinc ions a strong adsorption capacity for the monolith at low concentration of ZIF-8 precusor (19.5 μM, 10 mL). The adsorption content reached 9.7 wt% at a flow rate of 1.5 mL min^{-1} and a pump injection time of 30 minutes. Combining with the discussion above, it is feasible that the coated amount of MOF and the surface area of the monoliths can be regulated by both the pump injection time and flow rate on a need basis.

Table 3-3. The amount of zinc at different flow rate and pump injection time.

Flow rate（Time）	Zn (wt. %)
1 mL min^{-1}(10 min)	6.7
1 mL min^{-1} (20 min)	7.3
1 mL min^{-1} (30 min)	8.1
1 mL min^{-1} (40 min)	8.5
0.2 mL min^{-1} (30 min)	6.2
0.5 mL min^{-1} (30 min)	7.5
1.5 mL min^{-1} (30 min)	9.7
1.5 mL min^{-1} (20 min)	8.5

Stress-strain behavior

Uniaxial compression deformation tests were performed to assess the influence of ZIF-8 layers on the mechanical strength of the C-*g*-PSS monolith. As can be seen in Figure 3-6, after the deposition and growth of ZIF-8 on the surface of the skeleton, the monolith exhibited four times higher compressive stress than the C-*g*-PSS monolith at

60% strain, and the compressive modulus increased from 3.4 MPa to 10.2 MPa. Moreover, the ZIF-8@PSS monolith showed considerable improvement in terms of stiffness possibly because the ZIF-8 acted as a reinforcement material.

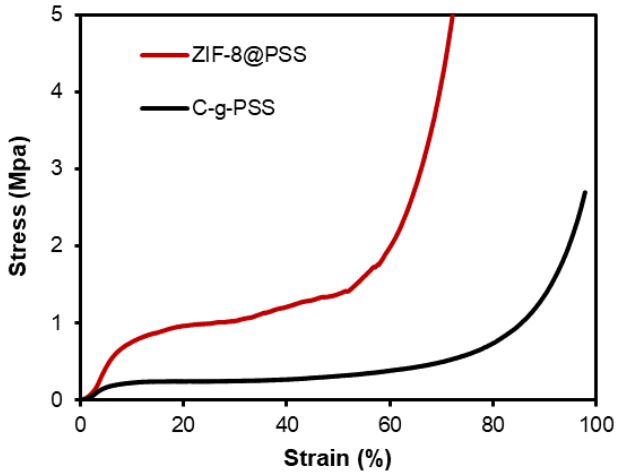

Figure 3-6. Compression stress-strain curves of C-*g*-PSS and ZIF-8@PSS monoliths.

Evaluation of permeability

The average measurements of pressure loss at a water flow rate of 1, 2 and 3 mL min^{-1} were successively used to calculate the permeability coefficient B_0. In order to reduce the deviation caused by backpressure, the pressure loss was analyzed by utilizing the average of the three measurements. As can be seen in Figure 3-7, with a ZIF-8 coating, the permeability of the monolith will be reduced, and the reduction will be more pronounced in case the flow rate or pump injection time are increased. The explanation for this phenomenon is simple; increasing the flow rate or pump injection time subsequently increases the amount of monolith interface in contact with ZIF-8. ZIF-8 was allowed to grow on the internal skeleton of the monolith layer by layer. It is the gradually thickened ZIF-8 layers that narrowed the monolith pores, thereby reducing the permeability. Author has noticed that there was a linear increase in the pressure drop as the flow rate increased for both the C-*g*-PSS and ZIF-8-coated composite monolith. At

the same preparation time (30 min) of ZIF-8@PSS monoliths, the faster the flow rate, the higher the resulting backpressure. This phenomenon was also observed at the different pump injection times at same flow rate (1.5 mL min^{-1}) in the sense that the longer the pump injection time, the higher the backpressure. Optimization of the flow rate and pump injection time is vital in practical application as it ensures the monolith structure will not collapse in the event of significant pressure drop. Meanwhile, coating with adequate and homogeneous MOF layers is also important.

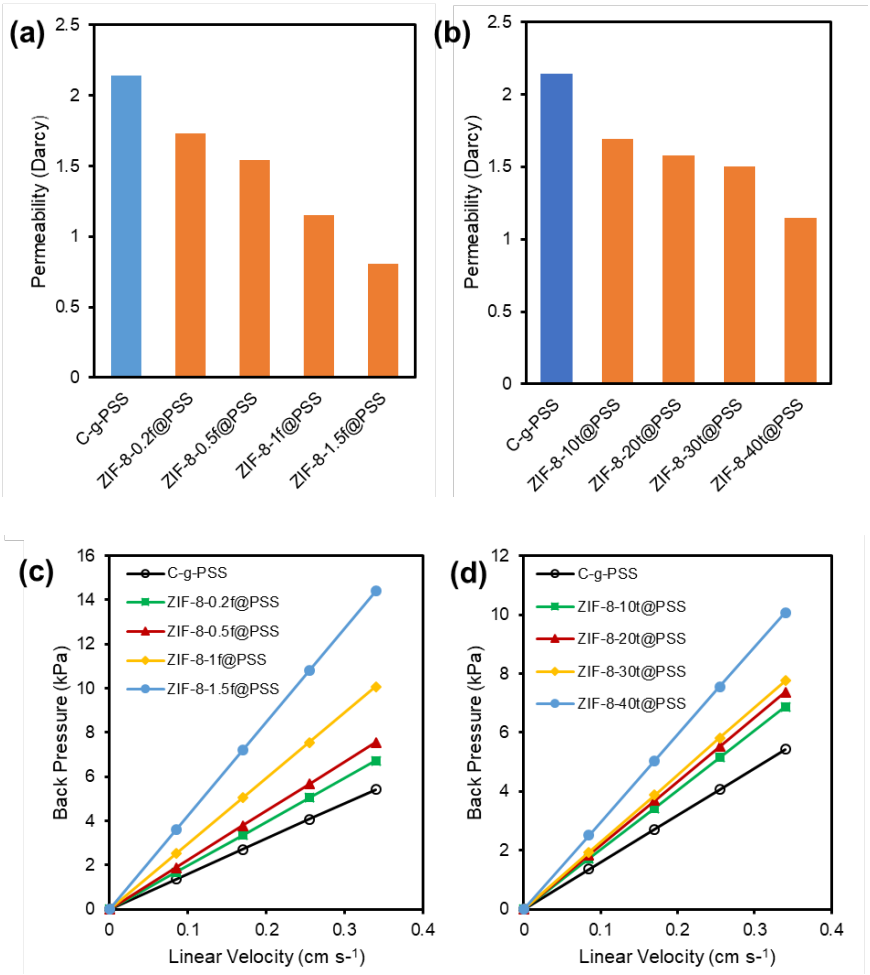

Figure 3-7 (a, b) Average permeability measurements of C-*g*-PSS and ZIF-8@PSS monoliths at flow rate of 1, 2 and 3mL min^{-1}; **(c, d)** Calculated back pressure at different linear velocity. (D: 5 mm, L:10 mm).

Heterogeneous catalysis in a microreactor format.

ZIF-8 has been noted to be an effective catalyst for Knoevenagel condensation reaction, which is an important synthesis route for fine chemicals and many pharmaceuticals. Research has established that catalyst loading is positively correlated to quantitative conversion rate.[12,13] Meanwhile, it is possible to regulate the ZIF-8 particles loaded in our monolith by increasing the pump injection time and flow rate. In this stage, author prepared a C-*g*-PSS monolith in a 100 mm-long tubing with an inner diameter of 5 mm, and coated it with ZIF-8 using the pump injection method at a flow rate of 1.5 mL min^{-1} for 30 min. This was done to exemplify its use as a micro flow-through reactor for catalyzing the Knoevenagel reaction of benzaldehyde with ethyl cyanoacetate (Figure 3-8 a).

Firstly, a batch reaction was conducted to assess whether there are any comparisons between ZIF-8 crystals and the ZIF-8@PSS monolith for the purpose of revealing the role ZIF-8 plays in the catalytic reaction. As shown in Table 3-4, for the same amount of ZIF-8, the ZIF-8@PSS monolith exhibits similar catalytic activity as the ZIF-8 crystals. Knoevenagel condensation reaction with ZIF-8-free PSS monolith provided the conversion of 8.4 % benzaldehyde and a desired product yield of 3.0 % at the reaction time of 30 min. ZIF-8 is regarded as an efficient base catalyst which originates from the 2-methylimidazole ligand. Author also established that the presence of the ZIF-8@PSS monolith in the flow microreactor speeded up the reaction rate and almost attained complete conversion after only 5 min, which is more than 3 times as high as with the batch condition (Figure 3-8 b).

The leaching of catalytic particles is the most censorious flaw of continuous-flow microreactors because it will eventually lead to momentous catalyst loss and

contamination of the product stream. Figure 3-8 c shows details of the analysis of the stability and reusability of the ZIF-8@PSS monolith microreactor. It can be seen that there was 99% catalytic conversion for the first 5 times, and only decreased by 4% past the 10th time. The actual amounts of ZIF-8 before and after 10 recycling times were analyzed through ICP-MS. The results showed that negligible reduction of Zn was obtained (before: 9.70 wt.%, after: 9.69 wt.%). The slow decrease in catalytic performance might be due to some micro pores/channel in monolith are closed due to the continued back pressure in the flow process. In addition, negligible reduction of Zn was detected, indicating that almost no catalyst loss during the experiment. It is anticipated that the majority of the catalytic activity takes place on the surface of the ZIF-8 crystals. The C-*g*-PSS monolith itself has a certain catalytic ability compared with blank (＜2%), the integration of ZIF-8 and C-*g*-PSS monolith thereby intensifies the catalytic activity in flow reaction. This form of nanoparticle encapsulation in C-*g*-PSS monolith can also be applied in other catalytic processes.

Table 3-4. Benzaldehyde conversion of 20 mg ZIF-8@PSS monolith (about 1.9 mg ZIF-8), 1.9 mg bulk ZIF-8 and 20 mg C-*g*-PSS monolith for 9 mL reactant mixture in the batch reaction

Sample	Reaction time (min)					
	5	10	15	20	25	30
ZIF-8@PSS	48.7 %	75.3 %	81.6 %	83.9 %	84.5 %	85.9 %
Bulk ZIF-8	49.3 %	74.0 %	80.8 %	83.5 %	84.8 %	85.0 %
C-*g*-PSS	0.3 %	5.0 %	6.5 %	7.2 %	7.8 %	8.4 %

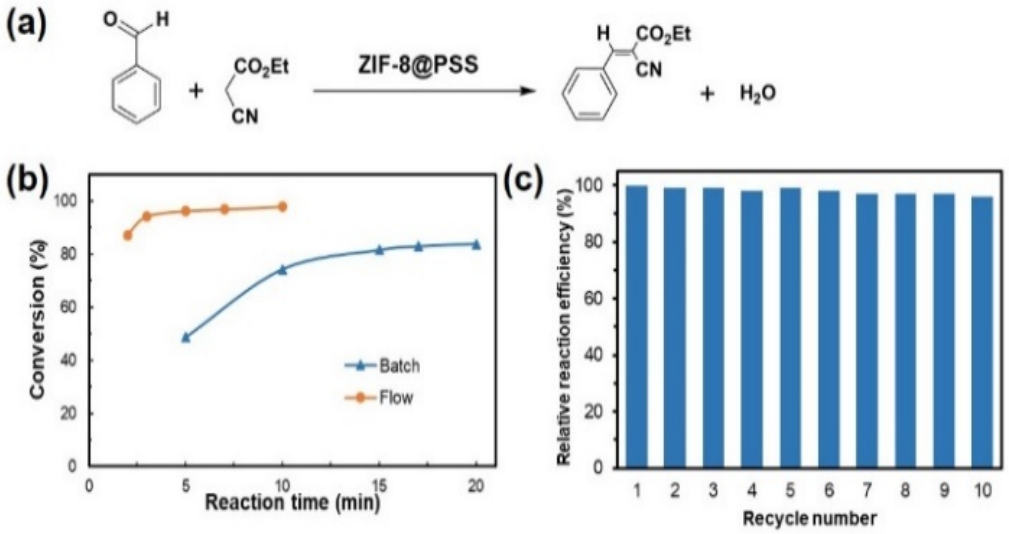

Figure 3-8 (a) Knoevenagel reaction of benzaldehyde with ethyl cyanoacetate (Reaction conditions: 20 mg of ZIF-8@PSS monolith, calculated ncatalyst=0.03 mmol, 32 mmol of benzaldehyde and 32 mmol of ethyl cyanoacetate in DMSO at 60 °C; **(b)** Conversion of the Knoevenagel condensation reaction in flow mode and batch catalysis mode using ZIF-8@PSS monolith microreactor; **(c)** The reusability of ZIF-8@PSS monolith for Knoevenagel reaction.

This reaction was also authenticated by H^1NMR. As shown in Figure 3-9, the corresponding peaks of reactant benzaldehyde at 9.96 ppm as well as those of ethyl cyanoacetate at 3.92 ppm basically vanished in the spectrum of products, which shows that benzaldehyde had completely reacted. ZIF-8@PSS monolith microreactor achieved the highest conversion of benzaldehyde up to 99 %, and yield of the desired product up to 93 % after reaction time of 20 min. Compared with batch reaction (TOF= 609 h^{-1}), this microreactor exhibited extremely high catalytic efficiency (TOF=4616 h^{-1}, almost 7 times higher than batch reaction) and long-term stability. The enhanced catalytic performance of the ZIF-8@PSS monolith can thus be credited to the augmentation of the reaction rate by the microreactor and the greater efficiency of the nanosized ZIF-8 crystals coated on the monolith.

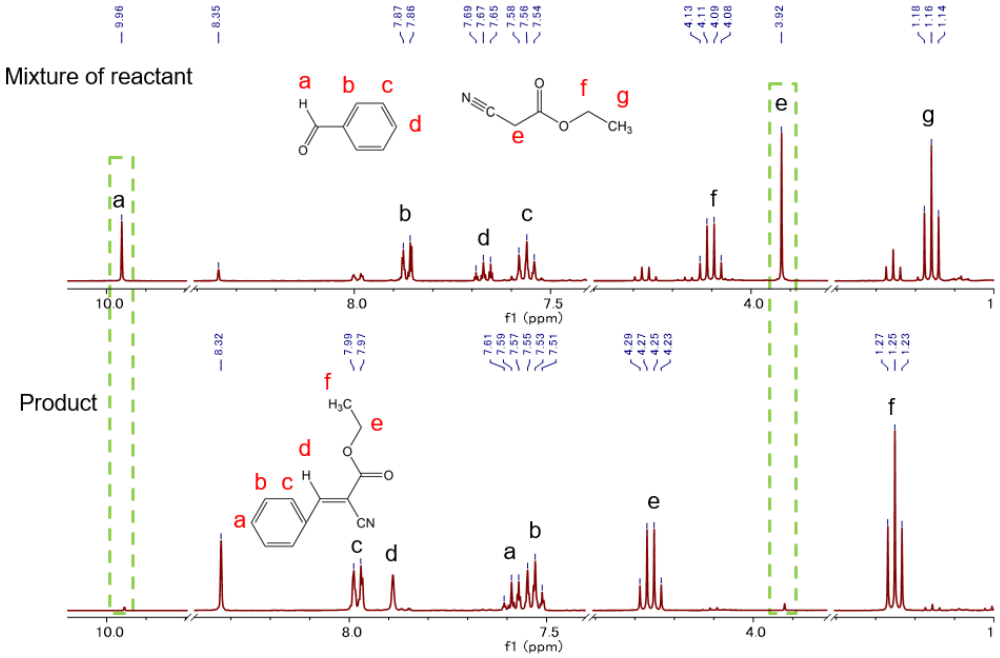

Figure 3-9. H^1NMR spectrum of reaction agents and product of the Knoevenagel condensation reaction.

Preconcentration of micropollutants from water in short column format.

To examine the reproducibility and solid-phase extraction of toxic water micropollutants, a short ZIF-8@PSS monolith column of 5 mm length × 5 mm i.d. was prepared. It demonstrated to have minimal back pressure high flow rate during the flow-based extraction process. Preconcentration factor (PF) and extraction recovery (ER) as analytical responses were calculated based on the following equations:

$$PF = \frac{C_{sedimented}}{C_0} \qquad (1)$$

$$ER\ (\%) = \left(\frac{V_{sedimented}}{V_{sample}}\right) PF \times 100 \qquad (2)$$

where, PF, $C_{sedimented}$ and C_0 are the preconcentration factor, analyte concentration in the sedimented phase and initial analyte concentration in the sample, respectively; ER (%), $V_{sedimented}$ and V_{sample} are the extraction recovery, volume of the sedimented phase and volume of the sample, respectively.

For the practical experiment, bisphenol A and 2,4-dichlorophenol were selected as sample micropollutants. They were extracted from an aqueous solution and then eluted with an organic solvent before quantification using HPLC. The enrichment of the micropollutants was monitored by examining an increase in the extracted quantity after the sample volume flowing through the column was increased (shown in Figure 3-10). Using the ZIF-8@PSS monolith allowed the micropollutants to be detected even at very low levels, something that was not possible with direct analysis. It is also worth noting that the extraction flow rate is a very significant factor in this process. The extraction of BPA and 2,4-DCP was conducted at flow rates of up to 3 mL min^{-1} to ensure there was no high back-pressure or leakage of ZIF-8. An exemplary performance was achieved with all the flow rates as shown in Figure 3-10 b. The retained pollutants were then liberated with 500 μL of high-purity chromatographic solvent before proceeding with HPLC analysis. This procedure ensures that no polluted water comes into contact with the chromatographic equipment as it could spoil it.

Some of the parameters that could affect the sensitivity and reproducibility of the monolith include the elution volume and flow rate. As can be seen in Figure 3-10 c and d, the retained micropollutants can be eluted with just 0.3 mL of solvent as increasing the solvent volume to 0.5 mL has no remarkable impact. This small volume evinces that the use of organic solvents necessary for the effective desorption of pollutants and concurrent regeneration of the support for the next extraction is reduced. It is important to mention that desorption also occurred at flow rates as high as 2 mL min^{-1} and the extraction efficiency remained almost the same, meaning there was a reduction in the total extraction time. Another advantage of this ZIF-8@PSS monolith is the facile and complete regeneration when the extracted pollutants are eluted with an organic solvent,

such as acetonitrile. This was proven by conducting 10 consecutive extractions and the error margin was below 1% for both BPA and 2,4-DCP (Figure 3-11).

Author believes that preconcentration is also enhanced by the facile coating of desired MOFs with different morphologies and functionalities. This can be convenient for selective extraction, which allows the use of different metal-ion-based MOF precursors. These changes do not need any unique synthetic skills or additional facilities to prepare or reduce the entire preparation time.

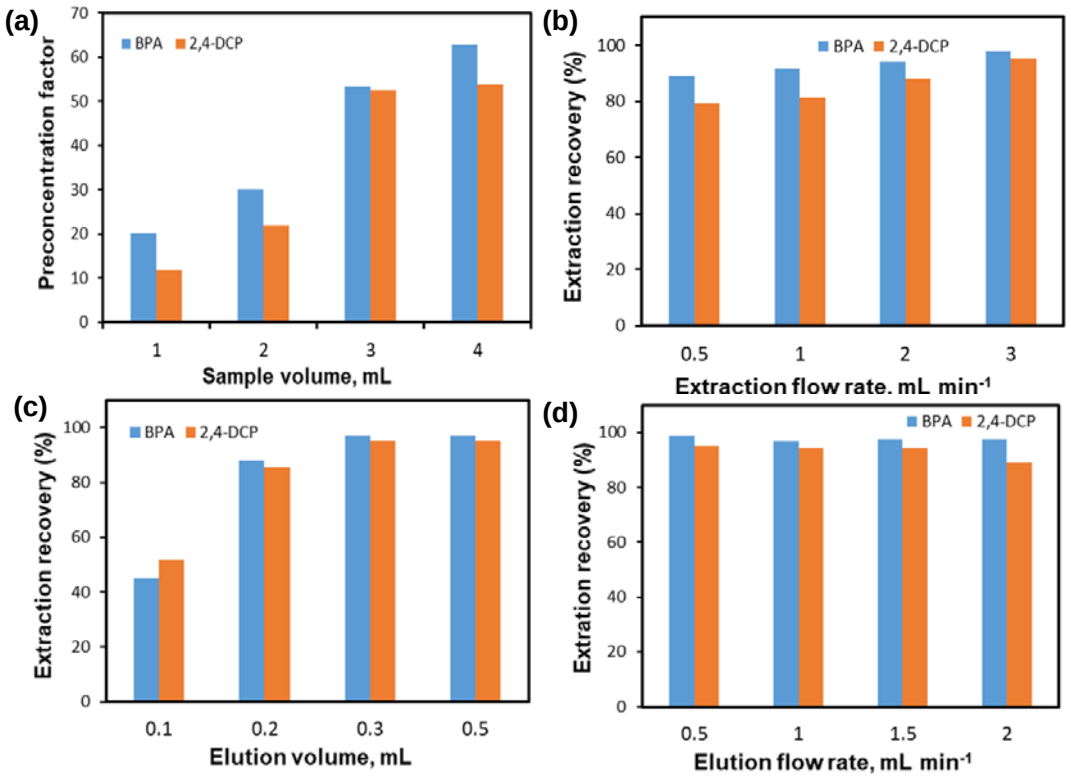

Figure 3-10 (a) Preconcentration factors obtained using different sample volumes on the extraction of BPA and 2,4-DCP using the ZIF-8@PSS monolith. Extraction flow rate, 1 mL min^{-1}; **(b)** Effect of the extraction flow rate. Sample volume, 2 mL. Analyte concentration, 100 µg L^{-1}; eluent volume and composition, 1mL of acetonitrile; elution flow rate, 1 mL min^{-1}; **(c)** Effect of the eluent volume. Elution flow rate, 1mL min^{-1}; **(d)** Effect of the elution flow rate. Analyte concentration, 100 µg L^{-1}; extraction flow rate, 2 mL min^{-1}; elute, 0.5mL of acetonitrile; Sample volume, 2 mL.

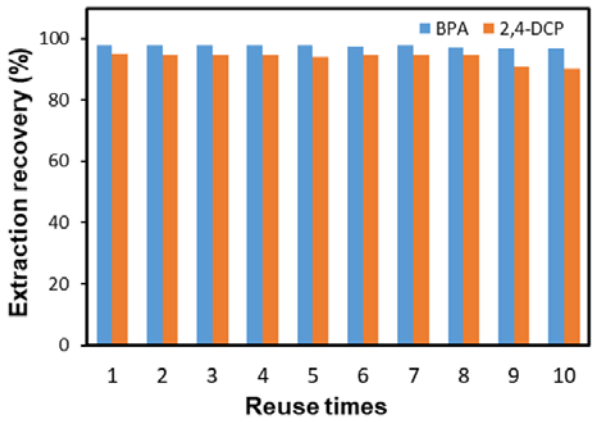

Figure 3-11. Reusability of ZIF-8@PSS monolith for extraction of BPA and 2,4-DCP. Analyte concentration, 100 μg L^{-1}; extraction flow rate, 2 mL min^{-1} eluent volume and composition, 0.5 ml of acetonitrile; elution flow rate, 1.5 mL min^{-1}; Sample volume, 2 mL.

3.4 Conclusion

To conclude, in this study, a modest and articulate approach for the anchoring MOFs within the pores of monolithic macroporous polymer structures with exposed pre-defined chemical moieties have been proposed. The proposed strategy is acquiescent to fast preparation of nanoparticle/polymer monolith conjugates under mild conditions. By taking advantage of the affinity of Zn^{2+} ions for multiple sulfonate moieties, author examined how the ZIF-8 coating can be enhanced through a pump injection method. These plastic composite materials have been reported to be effective for flow-through microreactor catalysis and extraction of micropollutants. As a catalysis microreactor, ZIF-8 can provide for quicker and higher conversion while maintaining outstanding stability and reusability. Automated operation characterized by low back-pressures can be achieved by utilizing preconcentration or selective extraction of environmental micropollutants that is centered on flow-through techniques. Based on the affinity of metal ions of MOFs for anionic sulfonate moieties, author believe the proposed approach

can prove beneficial for the propulsion growth of other MOFs on anionic polyelectrolyte modified polymer monolith in a rather controllable manner.

3.5 References

1. Pastre J C, Browne D L, Ley S V, *Chem. Soc. Rev*, 2013, **42**, 8849-8869.
2. Melchert W R, Reis B F, Rocha F R P, *Anal. Chim. Acta*, 2012, **714**, 8-19.
3. Darder M, Salehinia S, Parra J B, *ACS. Appl. Mater. Interfaces*, 2017, **9**, 1728-1736.
4. Shekhah O, Fu L, Sougrat R, *Chem. Commun*, 2012, **48**, 11434-11436.
5. Fu Y Y, Yang C X, Yan X P, *Chem. Commun*, 2013, **49**, 7162-7164.
6. Lu G, Li S, Guo Z, *Nat. Chem*, 2012, **4**, 310.
7. Pan Y, Liu, Y, Zeng G, *Chem. Commun*, 2011, **47**, 2071.
8. Cravillon J, Münzer S, Lohmeier S J, *Chem. Mater*, 2009, **21**, 1410-1412.
9. Barankova E, Tan X, Villalobos L F, *Chem. Int. Ed*, 2017, **56**, 2965-2968.
10. Rafti M, Allegretto J A, Segovia G M, *Mater. Chem. Front*, 2017, **1**, 2256-2260.
11. Liu J, Wöll C, *Chem. Soc. Rev*, 2017, **46**, 5730-5770.
12. Tran U P N, Le K K A, Phan N T S, *ACS. Catalysis*, 2011, **1**, 120-127.
13. Ghani M, Maya F, Cerdà Victor, *RSC. Adv*, 2016,**10**, 48558-48565.

Concluding Remarks

In this doctoral dissertation, cellulose-based functional monolith with various functional properties were studied. Cellulose monoliths possess unique 3D-network porous structure with high permeability and thus can be used to prepare functional or composite monoliths for flow-based applications. Such cellulose-based functional or composite monoliths maintained the superior chemical and physical attributes of cellulose monolith while preserving the functional properties of modification moieties. The results obtained through this dissertation are summarized as follows.

In chapter 1, a simple green synthetic methodology of effective cationic functionalization of cellulose monolith using environmentally benign deep eutectic solvents (DES) was proposed. DES (chlorocholine chloride/urea), as a reaction medium, act as both functionalization reagent and solvent. The obtained DES-modified cellulose monolith exhibited great adsorption capacity and that it could bind with the anionic dyes quickly and strongly. Moreover, high dye recoveries were achieved using appropriate desorption conditions and the dye removal process only consumed no more than 1 hour to complete the adsorption and desorption cycle under a negligible pressure drop. The simpler large-scale design for ion exchange monolith-scale-up can be easily achieved by enlarging the monolith while the applied pressure is still low. This work may provide an instruction for preparing modified cellulose monolith in a more simple and green strategy.

In chapter 2, author proposed a versatile approach for both cationic and anionic modification of cellulose monolith via a simple free-radical polymerization of anionic and cationic monomers, respectively. Ion-exchange property endow this monolith with an ultrahigh adsorption capacity of cationic or anionic dyes from water. And high dye

recoveries were achieved using appropriate desorption conditions. Both kinds of the ion exchange monoliths have the benefit of saving energy as well as the reactive dye removal-time. It was found that C-*g*-PSS monolith exhibited greater adsorption capacity and removal efficiency and could bind with the cationic dyes more quickly and strongly compared with the C-*g*-APTAC monolith. However, the C-*g*-APTAC monolith achieved better dye recovery and regeneration ability. This work may open a way of grafting specific polymers based on designated adsorption or separation applications.

In chapter 3, functional composite monoliths with MOFs anchored within the pores of monolithic macro-porous polymer structures with exposed predefined chemical moieties was developed by using a quick and modest pump injection approach. These prepared nanoparticle/polymer composite monoliths with hierarchical porous structure have been reported to be effective for flow-through microreactor catalysis and extraction of micropollutants. Author believes the proposed approach can prove beneficial for the growth of other MOFs and coordination polymers on varied functional surfaces.

In summary, several kinds of functional cellulose monoliths were successfully prepared through various modification methods. These modified monoliths possessed suitable pore size, controllable permeability and with desired functional properties, these cellulose-based functional monoliths would find promising applications in various fields of flow-based mode. Furthermore, the versatile, low-cost synthetic routes for the preparation of porous monoliths will be expected to extend to other types of polymer sources.

List of Publications

1. Cationic Functionalization of Cellulose Monoliths Using a Urea-Choline Based Deep Eutectic Solvent and Their Applications

   Zhaohang Yang, Taka-Aki Asoh* and Hiroshi Uyama*

   Polymer Degradation and Stability, 2019, **16**, 126-135.

2. Removal of Cationic or Anionic Dyes from Water Using Ion Exchange Cellulose Monoliths as Adsorbents

   Zhaohang Yang, Taka-Aki Asoh* and Hiroshi Uyama*

   Bulletin of the Chemical Society of Japan, 2019, **92**,1453-1461.

3. A Cellulose Monoliths Supported Metal/Organic Framework as a Hierarchical Porous Material for a Flow Reaction

   Zhaohang Yang, Taka-Aki Asoh* and Hiroshi Uyama*

   Chemical Communications, 2020, **56**, 411-414.

Acknowledgments

This study was carried out from 2016 to 2019 at the Department of Applied Chemistry, Graduate School of Engineering, Osaka University. On finishing the PhD course, I'm really grateful for the kind assistance and support from all members around me during the three years.

First and foremost, I would like to express my deepest gratitude to my supervisor, Prof. Hiroshi Uyama, for his continuous guidance and invaluable discussion on my research. I would not be able to finish my study smoothly without his timely advice and kind-hearted encouragement. I also sincerely thank him for giving me a chance to attend the Bioplastic Global Joint Satellite Symposium held in Malaysia, MoDeST 2018 international conference held in Tokyo, and the second workshop for Korea-Japan young scientists. His keen and vigorous academic observations enlighten me in my future study and career.

I am profoundly grateful to Associate Prof. Taka-aki Asoh, for his expert advice and inspirations to improve the quality of my research. I also thank him for his efforts in knowledge sharing and manuscripts revising. Without his help, this thesis would not be possible.

I appreciate Assistant Prof. Takashi Tsujimoto for his heartfelt supports.

Special thanks to Ms. Yoko Uenishi and Ms. Tomoko Shimizu for their kind help and warm-hearted support.

I am very thankful to the past and present fellow labmates in Uyama Lab: Dr. Yu Shu, Dr. Qidong Wang, Dr. Tomonari Kanno, Mr. Zhengtian Xie, Mr. Chen Qian, Mr. Shunsuke Mizuno, Mr. Yusuke Hinamoto, Mr. Jiaji Yang, Mr. Haoyan Zhou, Ms. Yankun

Jia, Mr. Akihide Sugawara, Mr Yuya Higuchi, Mr. Ginga Hoshi, Ms. Yanting Lv, Ms. Hanyu Wen, etc. for their kind-hearted help both in my research and daily life.

The financial support from China Scholarship Council (CSC) for my academic study and my stay in Japan is greatly appreciated.

Finally, I would like to express particular appreciation to my parents, Ruihua Zhao, Jingyuan Yang and my boyfriend Zhihao Li for their endless support and love throughout my life. The warm encouragement from my family motivates me to persist in my research and study.

December 2019

Zhaohang Yang